UNIVERSITY OF LJUBLJANA
FACULTY OF MATHEMATICS AND PHYSICS
DEPARTMENT OF PHYSICS
MATHEMATICAL PHYSICS

Žiga Brenčič

Determination of working channels in the Aerogel RICH of the Belle II spectrometer

Master thesis

MENTOR: prof. dr. Peter Križan
CO MENTOR: dr. Rok Pestotnik

Ljubljana, 2020

UNIVERZA V LJUBLJANI
FAKULTETA ZA MATEMATIKO IN FIZIKO
ODDELEK ZA FIZIKO
MATEMATIČNA FIZIKA

Žiga Brenčič

Določanje delujočih kanalov v detektorju obročev Čerenkova pri spektrometru Belle II

Magistrsko delo

MENTOR: prof. dr. Peter Križan
SOMENTOR: dr. Rok Pestotnik

Ljubljana, 2020

Acknowledgements

I would like to thank both of my mentors prof. Peter Križan and dr. Rok Pestotnik for all their help with this thesis. Their infinite patience with me and my work was essential in writing this document. I would also like to thank dr. Andrej Gorišek for luring me into the world of particle physics and helping me with my first steps. In the end, I would not end up here if it were not for my parents, who have always encouraged my curiosity. Thanks, mum and dad.

Izvleček

V začeteku leta 2018 je na Japonskem v pospeševalniku SuperKEKB začel obratovati spektrometer Belle II. Ob pričetku delovanja je potrebno spektrometer in njegove komponente umeriti. V magistrski nalogi opišemo potek umeritve detektorja Čerenkovih obročev ali po angleško Aerogel Ring Imaging Cherenkov detector (ARICH). ARICH je sestavljen iz sloja aerogela in fotonskega detektorja, razdeljenega na 60480 kanalov. V delu raziščemo, kateri kanali fotonskega detektorja zaznajo fotone, tudi ko fotonov ni bilo, in kateri kanali fotonov ne zaznajo nikoli. Nato pregledamo vpliv takšnih kanalov na meritve Čerenkovega kota in kako se število napačno delujočih kanalov spreminja tekom obratovanja spektrometra Belle II.

Ključne besede: Čerenkovo sevanje, detektor obročev Čerenkova, umeritev, spektrometer, analiza podatkov, eksperimentalne metode in inštrumentacija v fiziki onsnovnih delcev.

PACS: 41.60.Bq, 29.40.Ka, 06.20.fb, 29.30.-h, 29.00.00, 07.05.Kf

Abstract

In 2018, the accelerator SuperKEKB in Japan and the Belle II spectrometer started their operations. At the beginning of a spectrometer operation researchers began the calibration process of all sub-detectors. In this master thesis we present the calibration of the Aerogel Ring Imaging Cherenkov detector (ARICH). ARICH sub-detector consists of an aerogel plane and a position-sensitive photon detector plane. We explore which channels of the photon detector detected photons when there were not any photons present and which channels have never detected any photons at all. Then we investigate how the number of none working channels changes throughout the Belle II spectrometer operation. In the end we explore how the none working channels influence the measurements of the Cherenkov angle.

Keywords: Cherenkov radiation, Cherenkov detectors, Standards and calibration, Spectrometers and spectroscopic techniques, Experimental methods and instrumentation for elementary-particle and nuclear physics, Data analysis.

PACS: 41.60.Bq, 29.40.Ka, 06.20.fb, 29.30.-h, 29.00.00, 07.05.Kf

Contents

List of figures

Chapter 1

Motivation

In 2008 the development of the SuperKEKB electron-positron collider and the Belle II spectrometer started. Different research groups from all around the world built Belle II spectrometer components. At the start of 2018 most of the parts were installed into the spectrometer. In March 2018 all sub-systems started the calibration phase.

The Belle II experiment will be running for seven years and during this time the sub-systems will sustain radiation damage. Radiation will degrade their initial performance. But to preserve the quality of produced data used for physics studies, each sub-system of the spectrometer has to be monitored, serviced and calibrated to maintain the optimal performance.

SuperKEKB collides beams of electrons and positrons to produce B mesons. Once B mesons decay, the decay products are detected and identified by different Belle II sub-systems. One of the particle identification devices in the Belle II spectrometer is the Aerogel Ring Imaging Cherenkov counter (ARICH).

ARICH uses the Cherenkov effect to determine the identity or mass of charged particles produced by B meson decays. Each Cherenkov photon generated by charged particles is then detected by one of the 60480 pixels of the position-sensitive photon detector plane.

At the beginning of the 2018 calibration, ARICH sub-system group observed that specific pixels of the photon detector never detected any photon hits (were dead) and that some of the pixels were detecting photon hits too often (were hot).

Goal of this master thesis is to develop a calibration procedure that allows us to identify the pixels of the position-sensitive photon detector that are misbehaving.

Chapter 2

Experiment

2.1 Physics program

The Belle II experiment is part of the SuperKEKB collider located in Tsukuba, Japan. Collider was developed to produce a large number of B mesons. During its operation, the Belle II experiment will gather 50 times more data than its predecessor Belle did. A large data set of measured B-meson decays will allow researchers to perform:

- high precision flavour physics measurements,
- detailed studies of cases where charge-parity (CP) is violated,
- measurements of CKM matrix elements,
- searches for the deviations from the Standard Model and
- measurements of rare decays of B, D mesons, and τ leptons.

2.2 SuperKEKB: B meson factory

SuperKEKB's main accelerator tunnel lies about 12 m below ground and has a diameter of 1 km. The accelerator's function is to collide bunches (groups) of positrons and bunches of electrons.

Electrons and positrons are produced in the linear injector and then accelerated with radio frequency (RF) cavities. After initial acceleration particles are sent into the accelerators ring.

The ring is constructed out of RF cavities, dipole magnets that bend the particles beams, and superconducting quadrupole magnets (QCS) that focus the particle beams. Along the SuperKEKB accelerator beamlines lies the Belle II spectrometer.

SuperKEKB accelerator is designed to achieve a beam focusing of 60 nm along y axis and 10 μm along x axis of the beamline. Such narrow focusing increases the

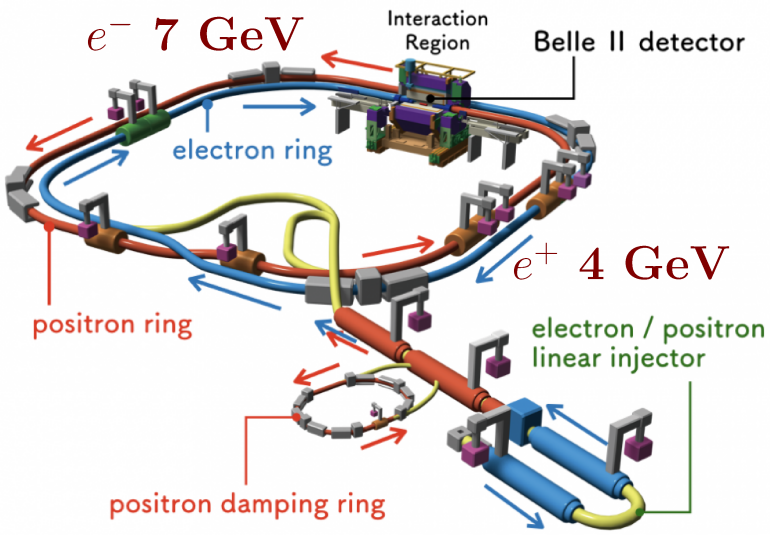

Figure 2.1: SuperKEKB collider and position of the Belle II spectrometer [1].

probability of e^+ e^- annihilation upon e^+ e^- bunch crossing.

When positron e^+ beam with the energy of 4 GeV and electron e^- beam with the energy of 7 GeV, collide particles annihilate and produce short-lived neutrally charged meson resonance. Resonance then decays into a pair of B mesons.

Since the energy of the electron beam is higher than the energy of the positron beam, the centre of the mass of the system is shifted in direction of the electron beam. Shift results in an asymmetric e^+ e^- collisions and after annihilation into boosted B mesons.

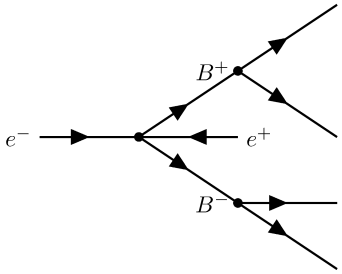

Figure 2.2: B meson production via e^+ e^- annihilation.

Those B mesons then decay into detectable products (mesons, baryons, fermions, photons) and undetectable products (neutrinos or other unknown particles). See Figure 2.2 for illustration of the e^+ e^- annihilation also called event.

2.3 The Belle II spectrometer

The Belle II spectrometer (see Figure 2.3) is constructed around the point where e^+ e^- beams collide (interaction point).

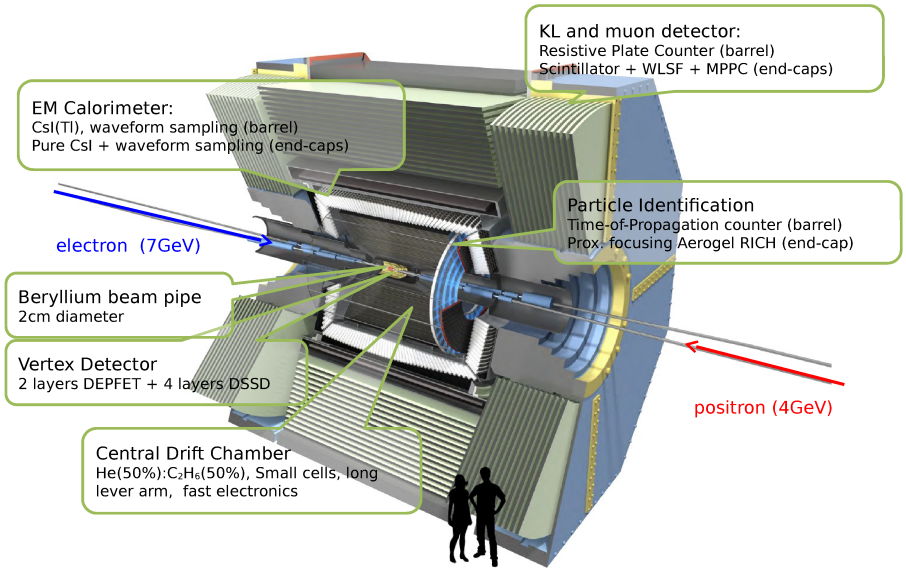

Figure 2.3: The Belle II spectrometer sketch [1].

The Belle II spectrometer uses a set of sub-systems to determine what happened after the e^+ e^- annihilation by measuring the properties of the decay products:

- particle charge and momenta,
- particle mass,
- particle energy.

Each sub-system can determine one or more of the particle properties. By combining all those measurements one can then reconstruct the physics that occurred after the e^+e^- collision.

The spectrometer has an onion-like composition of layers with different functionalities. Around the interaction point, the Belle II spectrometer uses data from Silicon Vertex Detector (SVD) and Silicon Pixel Detector (PXD) to determine the positions of the primary vertices (e^+e^- collision points) and the secondary vertices (points where mesons decay).

Next is the Central Drift Chamber (CDC) detector filled with a helium-based gas mixture that measures the curvature of charged particles trajectory in the magnetic field ($B = 1.5$ T). The CDC provides particle charge, particle momenta, and the energy loss $-dE/dx$ that charged particle sustained while travelling through CDC.

For particle identification, the Belle II uses two detectors based on the Cherenkov effect. The Time-Of-Propagation counter (TOP) is positioned in the barrel region of the spectrometer. The Aerogel Ring Imaging Cherenkov counter (ARICH) is located in the forward end-cap region.

To determine the energies of particles that interact via electromagnetic interaction the Belle II uses Electromagnetic calorimeter (ECL) constructed out of CsI(Tl) crystals. For detection of long-lived kaons, muons and neutral hadrons Belle II spectrometer uses scintillator based K_L-Muon (KLM) detector.

For the detailed spectrometer design see the technical drawing Figure 2.4.

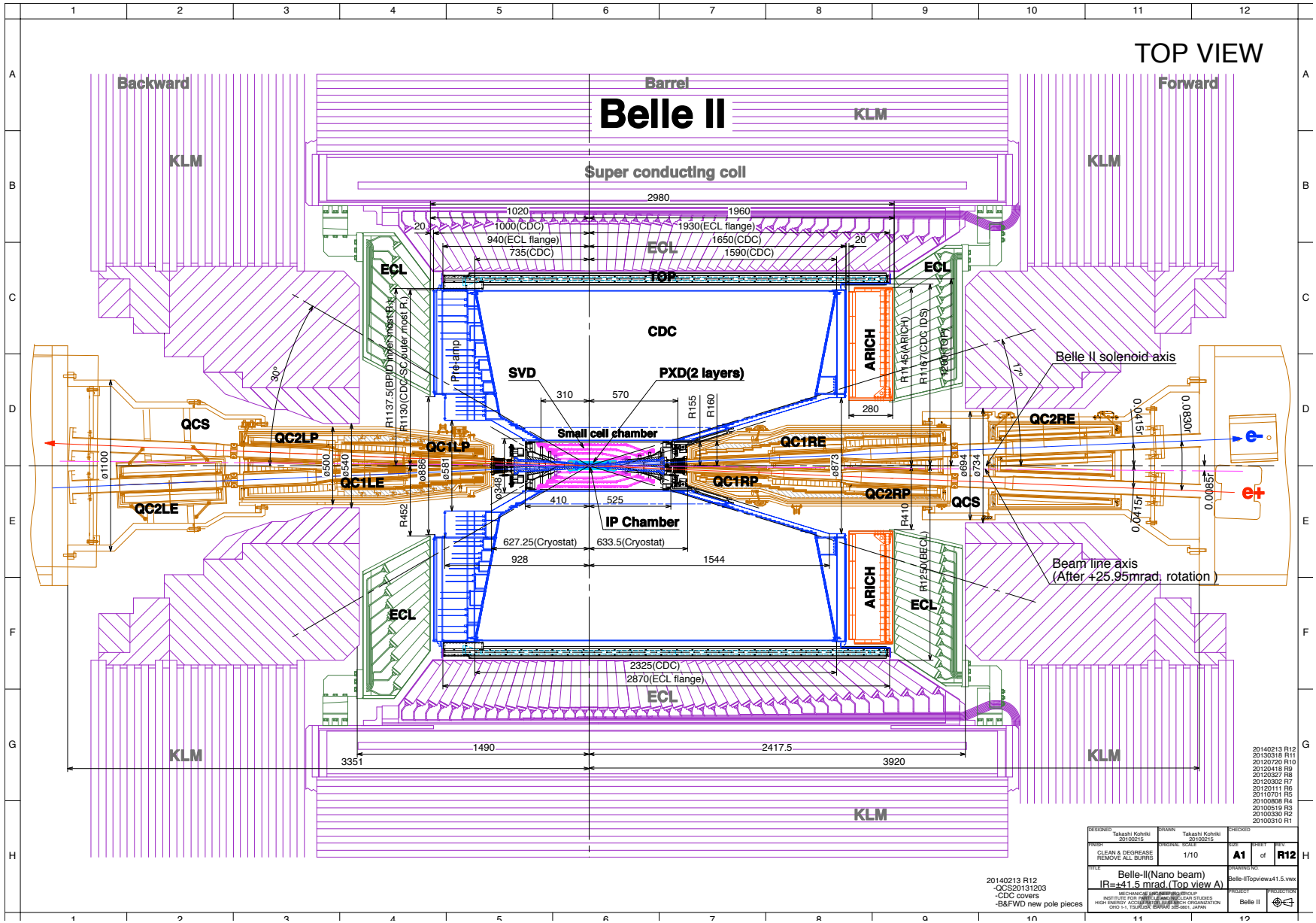

Figure 2.4: Technical drawing of Belle II cross section [1].

Chapter 3

Aerogel Ring Imaging Cherenkov counter (ARICH)

ARICH is one of the two sub-systems of the Belle II spectrometer that uses Cherenkov effect for particle identification. ARICH leverages Cherenkov effect to separate kaons from pions in the momentum region from 0.5 to 4 GeV/c. In the low momentum region from 0.5 to 1 GeV/c ARICH sub-system can also be used to separate muons from pions. The detector was developed by Experimental particle physics department of Jožef Stefan Institute from Slovenia and by several other research groups that are part of Belle II collaboration.

3.1 Cherenkov effect

When a charged particle travels through a material with velocity v higher than the speed of light in the medium, the charged particle produces electromagnetic waves that result in Cherenkov radiation or emitted photons. Photons are emitted under an angle called Cherenkov angle (see Figure 3.1 right). A similar effect happens when an aeroplane breaks the sound barrier. Plane creates a supersonic boom and a cone of sound waves (see Figure 3.1 left).

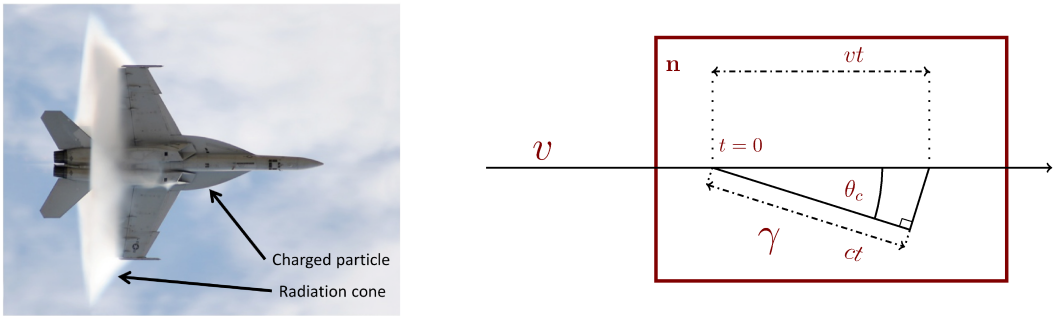

Figure 3.1: (Left) An analogue of Cherenkov effect with an airplane breaking the sound barrier and producing sound waves [2]. (Right): Sketch of a charged particle v travelling through the medium (with refractive index n) and emitting a photon γ under Cherenkov angle θ_c.

Marie Curie first reported about bluish Cherenkov light, but it was not util 1926 that French physicist Lucien Mallet observed the Cherenkov effect. In 1934 Pavel A. Cherenkov discovered the source of Cherenkov radiation [4]. The first detailed theoretical description was derived by Igor Frank and Ilya Tamm in 1937 [5]. Cherenkov, Frank, and Tamm received the physics Nobel prize in 1958 for their discovery. In 1940 Vitalii Lazarevich Ginzburg postulated a first quantum theory of Cherenkov radiation. Then in 1951, J.V. Jelley detected first high energy particles using Cherenkov radiation. Since then the Cherenkov effect is used for particle identification.

Frank and Tamm described in their theoretical work the Cherenkov radiation in the model of the isotropic medium, with zero conductivity and magnetic permeability $\mu = 1$. They neglected dispersion, reactions between atoms, scattering, and ionization. As a result of all these assumptions the charged particle travelling through matter has a constant velocity.

In the dielectric medium with refractive index n the speed of light $c = \frac{c_0}{n}$ is lower than speed of light in vacuum c_0. Frank and Tamm showed that the particle that travels through the medium with velocity v (that is greater than c) emits Cherenkov radiation. Velocity c is also called threshold velocity because it represents the boundary between the case where there is no Cherenkov radiation and the case where Cherenkov radiation is observed.

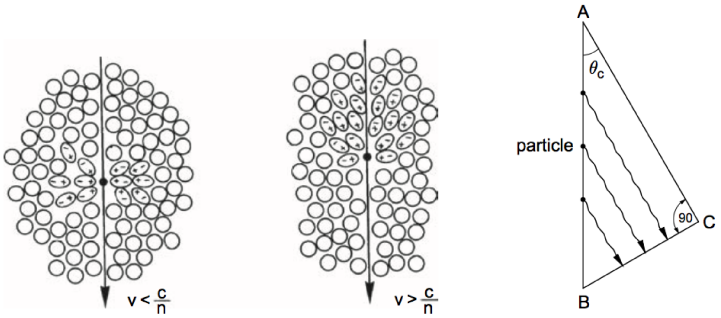

Figure 3.2: The distribution of dipoles in a dielectric medium produced by the passage of charged particle at low (left) and at high (middle) velocity. (Right) Cherenkov photons emitted under an angle θ_c by the charged particle [3].

On the microscopic level the following effect takes place. When a charged particle travels through the medium, it polarises the dipoles in the medium. The dipoles in the medium align with the charged particle (Figure 3.2 left). When a dipole relaxes, it emits a photon. If a charged particle is slower than the speed of light in the medium emitted photons interfere destructively and Cherenkov radiation is not observed. But if the particle travels with the speed faster than the speed of light in the medium, then dipoles do not manage to relax instantly. As a result, the photons start to interfere constructively and produce a light cone, also called Cherenkov radiation (See Figure 3.2 middle).

3.1.1 Cherenkov formula

The distance that charged particle travelled in the medium vt and the distance that the photon travelled in the medium ct form a right-angled triangle (see Figure 3.1 right). By using simple trigonometry and definition of c one obtains the formula for Cherenkov angle:

$$\cos\theta_c = \frac{ct}{vt} = \frac{c_0}{vn} = \frac{1}{\beta n} \qquad \beta = \frac{v}{c_0} \tag{3.1}$$

Or if we rewrite the formula to calculate the Cherenkov angle from particles momentum and mass:

$$\theta_c = \arccos\left(\frac{1}{n\beta}\right) \qquad \beta = \frac{p/c}{\sqrt{m^2 + (p/c)^2}} \tag{3.2}$$

From Jelley [6] we know that the number of the emitted photons N per specific charged particle can be approximated by:

$$N \approx d\left(1 - \frac{1}{n^2\beta^2}\right).$$

N is small (see Figure 3.9 for an example of the Cherenkov ring).

3.2 Detector design

The error of measured Cherenkov angle decreases with the number of emitted photons per charged particle. To improve our measurements, we want to increase the number of emitted photons per charged particle. Number of emitted photons increases if the thickenss of the medium that charged particle flies through is increased.

Inside the material the photons get emitted at different locations along the trajectory of the charged particle. If the material is thick, the photon emitted at the beginning of the material and the photon emitted at the end of the material will result in the measurements of different Cherenkov angles. No matter the fact that every photon is emitted under the same Cherenkov angle with respect to the charged particle track.

When thick material is used the photons that hit the detector plane, no longer form a thin ring (Figure 3.3 top) but a thick doughnut (Figure 3.3 middle). As a result, the resolution of the measurement of the Cherenkov angle drops. To overcome the spread of photons produced by a charged particle that flies through the thick material, one can use a multi-layer radiator (Figure 3.3 bottom).

Instead of having one thick layer with a fixed n (Figure 3.3 middle), we employ two radiator layers with $n_1 < n_2$ (Figure 3.3 bottom). If we compare the different

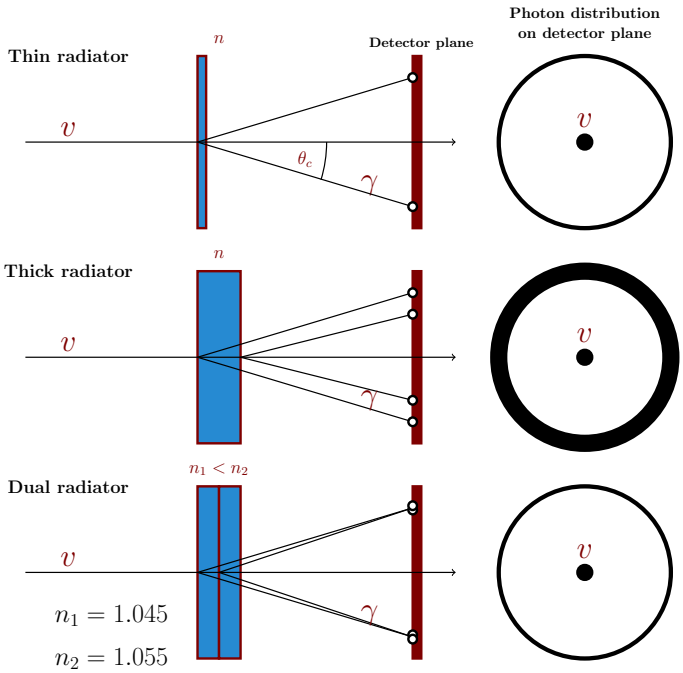

Figure 3.3: Comparison of different detector configurations for a thin (top), thick (middle) and dual radiator (bottom). (Left part): The structure of the radiator and corresponding Cherenkov photon angles with respect to the detector plane. (Right part): Cherenkov ring on the detector plane.

layer designs, we see that double layer radiator yields focused Cherenkov ring that contains more photons (see Figure 3.3).

By using two planes that are half as thick with different refractive indices the photons end up on the same ring. A focusing effect is achieved. It was observed in experiments that focusing configuration improves Cherenkov angle resolution.

But why not use more layers to get even better focusing? It was confirmed that with more layers, the Cherenkov angle resolution does improve. But the limiting factor in Cherenkov angle measurements is the spatial resolution of the position-sensitive photon detector. Because photon detectors resolution is worse than the photon spread in the Cherenkov angle adding more layers of the radiator does not yield any improvements.

3.2.1 Radiator material type

With ARICH we want to accurately distinguish between particles with momenta in the range $[0, 3.5]$ GeV/c. Refractive index of the radiator material determines the Cherenkov angle of emitted photons. Refractive index thus determines how accurately we can separate particles at different momenta p.

Cherenkov angle is a function of refractive index, momentum and mass $\theta_c(n, p, m)$ according to Eq. 3.2. To obtain the resolution band or how Cherenkov angle reso-

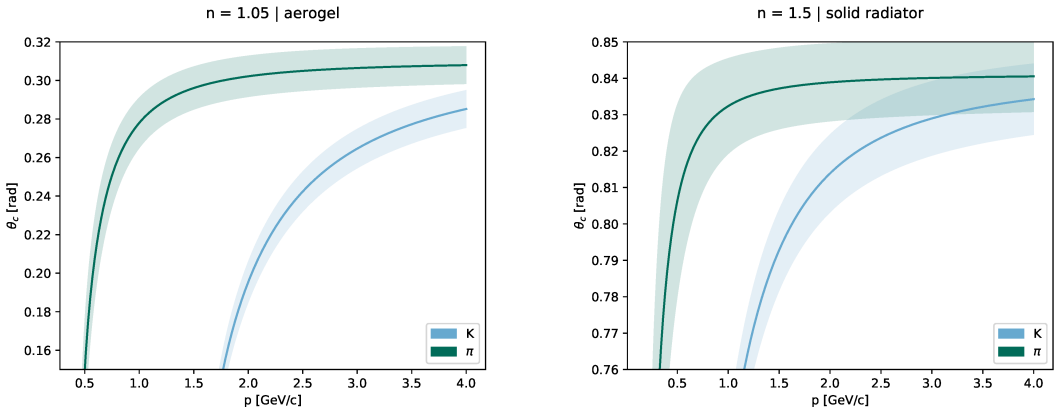

Figure 3.4: Cherenkov angle as a function of the momentum for π, K, for $n = 1.05$ (left) and $n = 1.5$ (right). Bands represent the error of measured Cherenkov angle ($\pm\sigma_{\theta_c}$).

lution changes with refractive index, momentum and mass, we can use Eq. 3.3. By using Cherenkov angle and resolution formula we can see how the Cherenkov angle differs for kaons and pions over larger momentum region for different refractive indices (see Figure 3.4).

From Figure 3.4 left we see that pion and kaon Cherenkov angles are well separated over the momentum region $[0, 4]$ GeV/c in the material with a low refractive index close to one: $n = 1.05$. For the material with high refractive index $n = 1.5$ (Figure 3.4 right), the Cherenkov angle increases, and the resolution bands begin to overlap at higher charged particle momenta.

To achieve good particle separation over the entire momentum region, ARICH uses two layers of material with the low refractive index. The material that allows fine-tuning of the refractive index to low values is aerogel. The aerogel is an amorphous, highly porous solid made of silicon dioxide (SiO_2). In the configuration of ARICH sub-system two different layers of aerogel are used.

3.3 Photon detector

Once the charged particle produces Cherenkov photons in the aerogel we need to detect them with a photon detector. But there are several requirements for the photon detector design that have to be met:

- operation in a high magnetic field of 1.5 T,
- ability to detect single photons,
- spatially segmented detector,
- resistivity to neutron radiation.

After extensive testing the Belle II collaboration decided that a suitable candidate

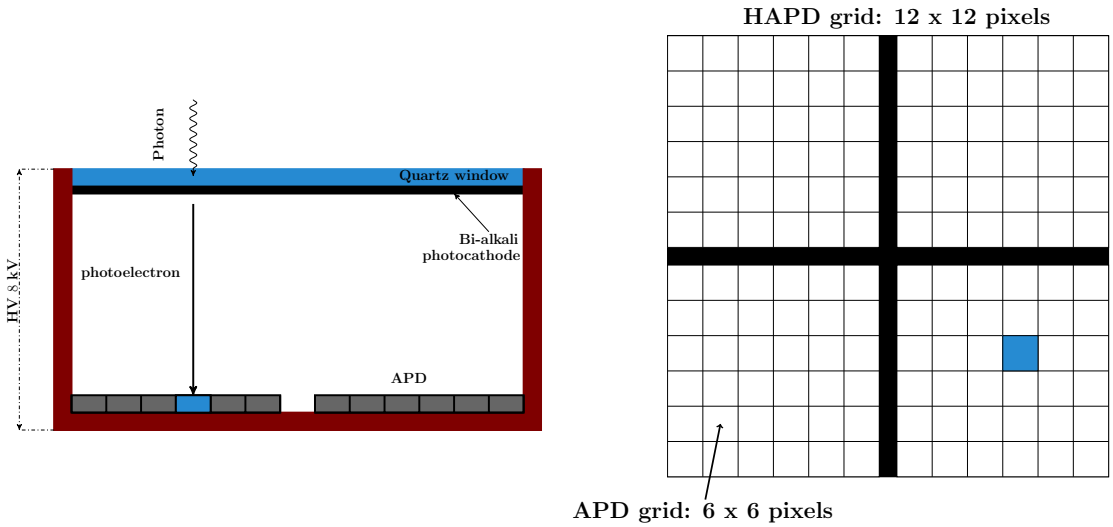

Figure 3.5: Left: Sketch of HAPD and photon conversion into an electron. Right: HAPD grid with a dead part of the material (black region) in the middle. The dead part of the material is not sensitive to photon detection and has the purpose of holding together the APD chips.

for photon detection purposes that meets all of the above requirements is Hybrid Avalanche Photon Diode (HAPD) see Figure 3.6.

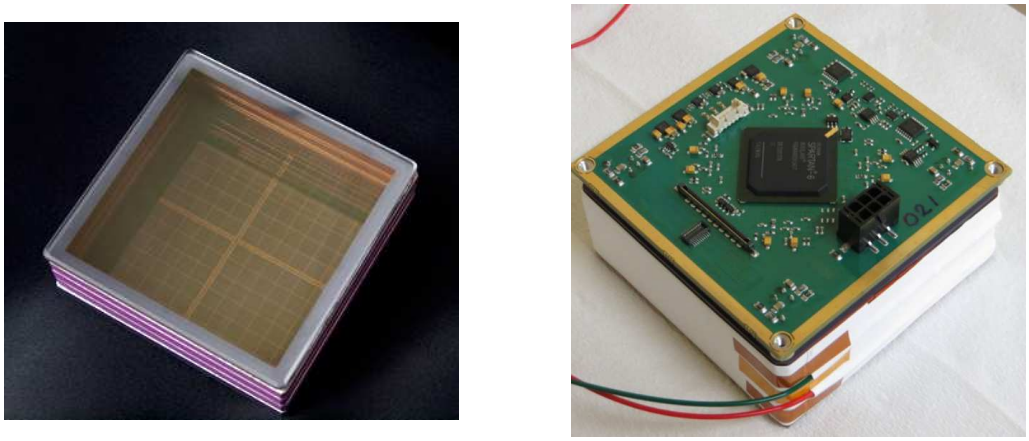

Figure 3.6: (left) Front side of the HAPD and (right) back side of HAPD with corresponding electronics [1].

Each HAPD is composed of 4 APD chips that each has 6 times 6 pixels. Pixels are silicon diodes of size 4.9 mm x 4.9 mm. To determine photons positions the HAPD leverages physics behind photo effect and the creation of electron-hole pairs in the semiconductor.

When the photon hits the photocathode on top of HAPD it produces a photo-electron via photo effect (see Figure 3.5). Produced photo-electron falls toward the APD and accelerates under the high electric field to the energy of around 10 keV. Once the accelerated photo-electron hits the silicon diode pixel in APD it produces

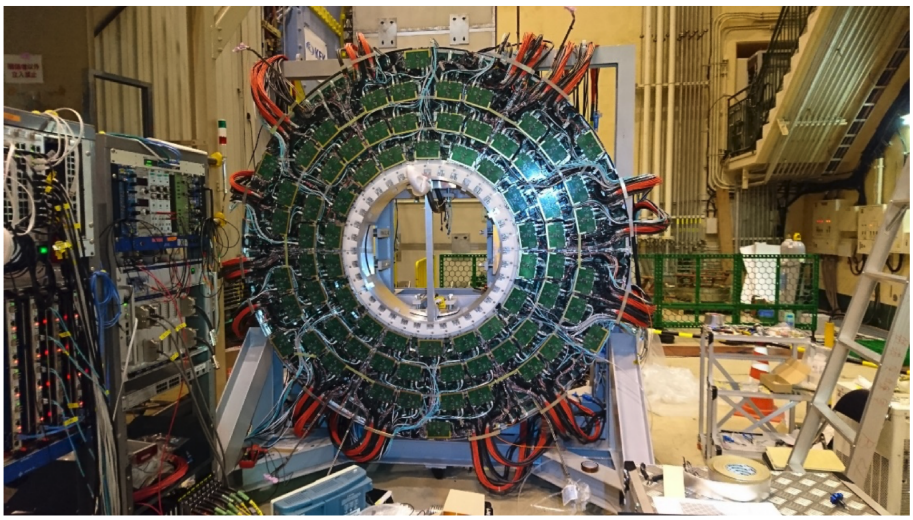

Figure 3.7: Electronics of the readout system at the back of the ARICH sub-system [1].

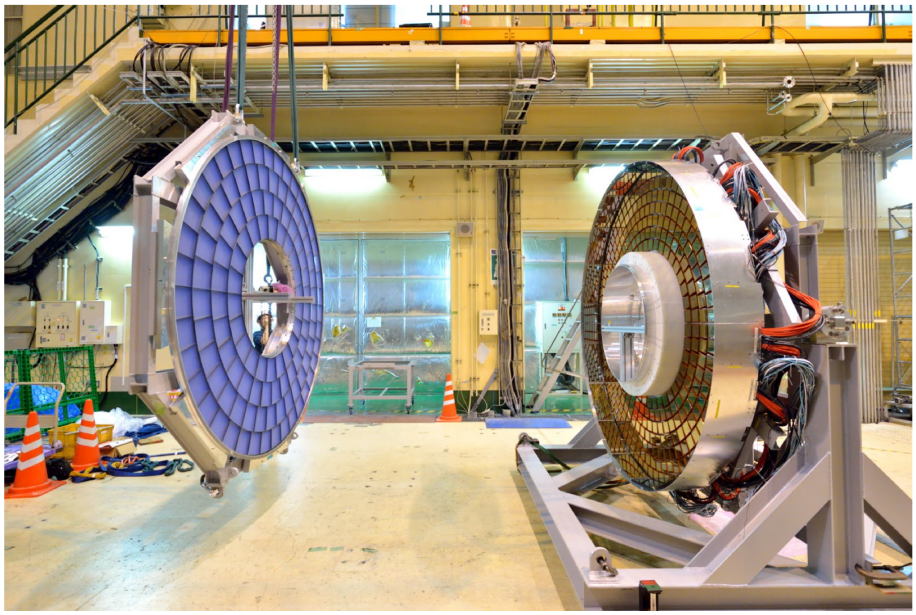

Figure 3.8: Installation of aerogel plane on the photon detector plane [1].

multiple electron-hole pairs. The HAPD electronics then determines which pixel was hit.

3.4 ARICH sub-system

With all ARICH components defined, we can now describe the full sub-system. ARICH consists of two planes. A position-sensitive photon detector plane and an aerogel plane that covers the photon detector plane.

Aerogel plane consists of two 2 cm thick layers of aerogel radiator with refractive indices $n_1 = 1.045$ and $n_2 = 1.055$, and an expansion volume of 16 cm. The photon detector plane consists out of 420 HAPD-s with 144 pixels per HAPD. That gives

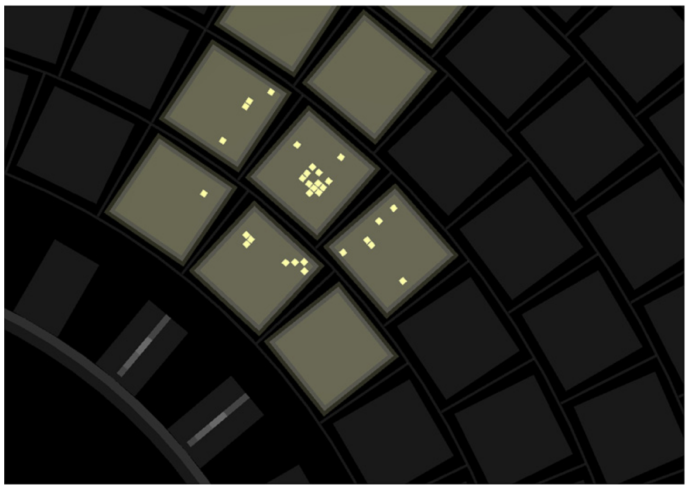

Figure 3.9: Cherenkov ring produced by a charged particle on the ARICH position sensitive photon detector plane [1].

us 60480 channels or pixels that can detect the position of the Cherenkov photon hits.

ARICH sub-system is located in a magnetic field of 1.5 T in the forward end-cap region of the Belle II spectrometer. ARICH covers 3.5 m^2 of the spectrometer area.

Electronics determines what pixels were hit. To read-out data from each APD, ASIC chips are used. Each ASIC chip has an amplifier, shaper and the discriminator to process the signal obtained from silicon diodes. Four ASIC chips are installed at the front end electronic board of each HAPD. HAPD ASIC-s are radiation hard and can be controlled through a field programmable gate array (FPGA).

HAPD front end boards are grouped in clusters of six. Each cluster sends data to a merger board that processes and transmits data out of the Belle II spectrometer. Once data for each Belle II sub-system gets out of the Belle II spectrometer it is sent to the computing farm and stored on the disks for further processing and physics analysis.

3.5 Cherenkov angle distribution

In our experiment a large amount of charged particles flies through our Cherenkov detector. Each charged particle produces a different amount of photons. Measured Cherenkov angle θ_c of each photon is slightly different.

For charged particles that fly trough ARICH (see Figure 3.10) we can compute θ_c if we know:

- the position of the photon hit on the detector plane,
- the distance that charged particle traveled between the aerogel and photon detector plane, and

- light refraction on the boundary: aerogel-air and boundary air-quartz glass.

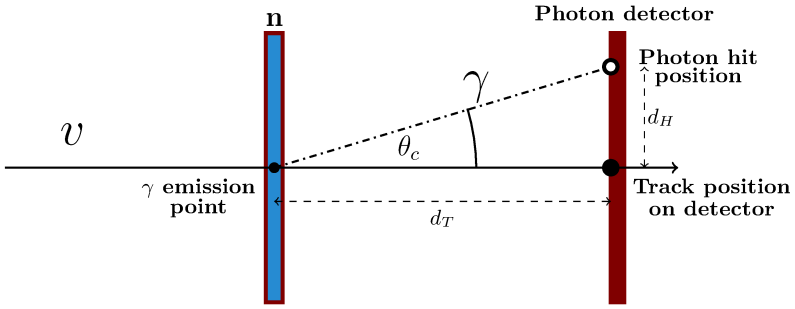

Figure 3.10: Photon hits the photonic detector under certain angle θ_c with respect to the point from which the photon was emitted.

If we compute the Cherenkov angle for each detected photon and each charged particle track and fill obtained angles into a histogram we obtain a Cherenkov angle distribution (see Figure 3.11). Distribution peak at ≈ 0.3 *rad* represents the mean measured Cherenkov angle.

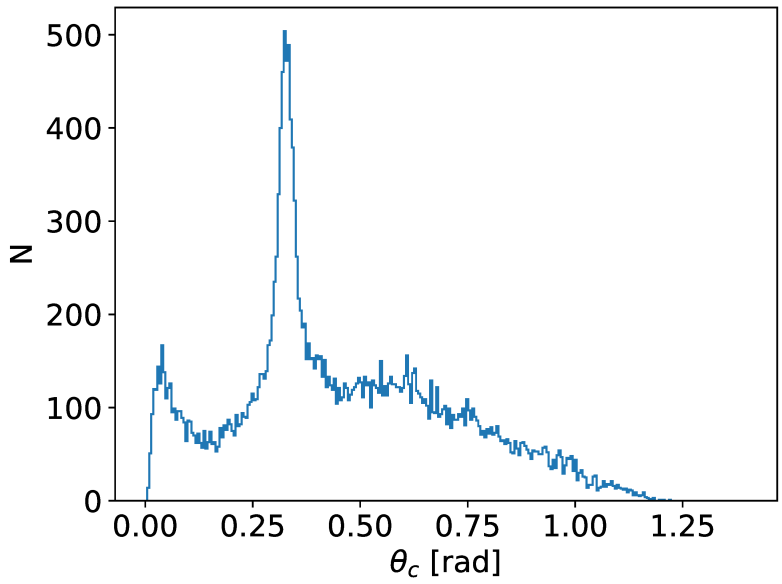

Figure 3.11: Example of Cherenkov distribution for photons produced by multiple charged particles.

The integral of the Cherenkov distribution normalized to the number of charged particle tracks gives us an average of emitted photons per charged particle track. Photons in the peak of Cherenkov distribution at 0.05 *rad* are produced when charged particle hits the photon detector plane and files through.

The resolution of the Cherenkov angle σ_{θ_c} is represented by the width of the Cherenkov distribution peak. σ_{θ_c} decreases a with number of emitted photons per charged particle track N and can be written as:

$$\sigma_{\theta_c} = \frac{\sigma_{\theta_{c_0}}}{\sqrt{N}}, \tag{3.3}$$

where $\sigma_{\theta_{c_0}}$ represents the single-photon resolution of the Cherenkov angle. $\sigma_{\theta_{c_0}}$ depends on radiator thickness, chromatic error, pixel size on the photon detector and on the error on the momentum of the particle track obtained from the tracking system.

3.6 Particle identification

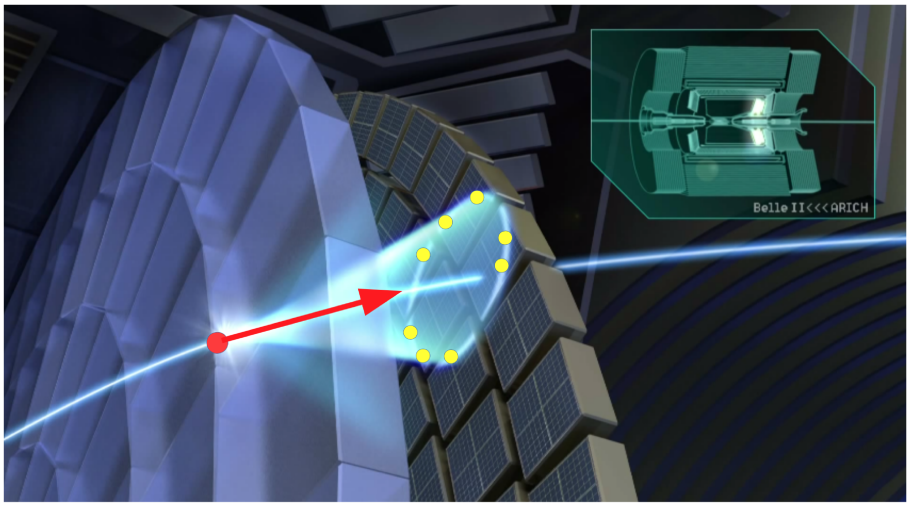

Figure 3.12: A charged particle with a specific momentum direction (red arrow) produces photons (yellow dots) in a shape of a cone on the ARICH photon detector plane[1].

When a charged particle flies through the aerogel plane it produces photons in the shape of a cone (see Figure 3.12). The response of ARICH gives us the location of produced photons while particles momenta is obtained from the Belle II CDC tracker.

Using the information about momenta and position of photon hits, we can construct a logarithm of the probability likelihood function $\log(L)$ for a hypothesis that the particle was a Kaon K or a hypothesis that the particle was a Pion π. In other words we check if its more likely that a particle with specific ARICH sub-system response and given momentum was K or π. We use $\log(L)$ instead of L because logarithm of the likelihood is numerically more stable then the likelihood itself. Details of the construction of the likelihood function can be found in [7]. In this section, we describe some of the effects of ARICH sub-system calibration on the likelihood function used in the distinction of kaons from pions.

For each charged particle with specific p that flies through ARICH sub-system we can calculate the logarithm of maximum likelihood function $\log L_K$ and $\log L_\pi$. Then

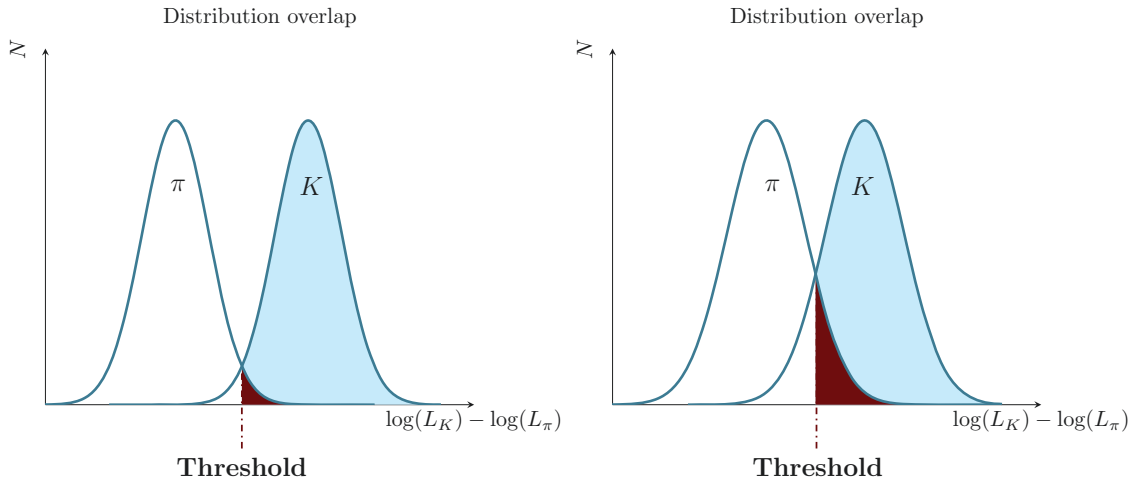

Figure 3.13: Overlap of distributions for a population of kaons and pions. Red region represents pions we misidentified as Kaons. The size of the overlap is defined by the position of the threshold. Distribution overlap when full knowledge about the detector is known (left) and overlap when the detector behaves differently than we assumed in our model (right).

we calculate the likelihood difference $\delta L(p)$ defined as:

$$\delta L(p) = \text{likelihood difference}(p) = \log L_K(p) - \log L_\pi(p) \tag{3.4}$$

We then fill $\delta L(p)$ values into a histogram (one histogram for each momentum p) and obtain Figure 3.13 (left). If the particle was a Pion, then L_K is small, and L_π is significant. $\delta L(p)$ is negative and results fall on to the left side of the distribution. If the particle was a Kaon then L_π is small and L_K is significant. $\delta L(p)$ is positive, and results fall to the right side of the distribution.

To define which particles are kaons and which pions we pick a value of $\delta L(p)$ and call it the threshold. Particles with $\delta L(p)$ smaller than the threshold are pions and particles with $\delta L(p)$ bigger then the threshold are kaons. But the distribution Figure 3.13 has an overlap in the middle. That's the region where we misidentify the particles (assign them the wrong identity). In this region we declare a certain amount of pions as kaons and part of kaons as pions.

To determine the efficiency of kaon identification we sum up the red and bluish region of Figure 3.13 and divide the sum with the Gauss that corresponds to kaons. We compute that value for every p. This gives us the pion misidentification probability as function of particle momentum p or percentage of pions that we identify as kaons.

When we computed $\delta L(p)$ for Figure 3.13 (left) we assumed that we knew everything about our sub-system. But in reality our sub-system could be misaligned. Detection channels could misbehave. So when we calculate the likelihoods and $\delta L(p)$ our model is slightly wrong. As a result our accuracy for π and K separation is worse than we modelled. We observe this as an increase in the overlap between π and K

population (see Figure 3.13 right). Larger overlaps in kaon-pion population result in higher misidentification probabilities.

To keep overlaps as small as possible we need to investigate how ARICH sub-system behaves over time. Then we can use that knowledge in physics analysis to improve the quality of the data. In other words, we need to monitor and continuously calibrate our sub-system to ensure the highest quality of the measured data.

Chapter 4

ARICH performance analysis

For the calibration of ARICH sub-system set of calibration tools that leverage the existing Belle II software infrastructure was developed. All of the calibration analysis programs were ran on KEK CC computing cluster in Japan.

Data used in the calibration studies is available at KEK CC cluster. Data is stored in batches called runs. During a single run the configuration of the Belle II subsystems is fixed.

4.1 Belle analysis software framework 2 (Basf2)

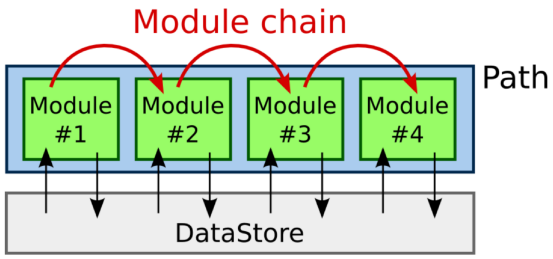

Figure 4.1: An example of a `basf2` processing chain that uses and creates `DataStore` objects. `Modules` are executed sequentially and pass data between each other [1].

The primary tool used in this thesis was Belle analysis software framework 2 [8]. `Basf2` is a modular `C++` data processing framework. The smallest unit of processing is `basf2.Module`. `Module`'s function is to perform a single task of reading and modifying event data.

Each processing `Module` has access to the database that contains settings for all Belle II sub-systems. On top of that each `Module` can have a set of control parameters used to modify module outputs from a higher-level code. Data is stored in

`DataStore` objects. In order to group modules that one wants to execute sequentially `basf2.Path` `python` object is used.

To store data objects to the disk `ROOT` CERN library [9] is used. Each module is written in `C++` then controlled via `python` steering file. An example of such `python` steering file is:

```
from basf2 import *

input_file = register_module("RootInput")
tracking = register_module("Tracking")
arich = register_module("ARICHReconstruction")
output = register_module("RootOutput")

# specify control parameters on modules if needed

main = create_path()
main.add_module(input_file)
main.add_module(tracking)
main.add_module(arich)
main.add_module(output)
process(main)
```

Steering file can be understood as a glue between `C++` modules that one wants to execute.

4.2 ARICH processing modules

Each of sub-systems has a set of processing modules and objects writen in `basf2`. In case of ARICH sub-system the following `C++` objects are implemented into the existing `basf2` framework:

- **ARICH Digits**: objects used to store which of ARICH 60480 pixels were hit in each measured or simulated event.
- **ARICH Hits**: module produces x, y coordinates from ARICH Digits object.
- **ARICH Info**: storage object for number of tracks and any other event data.
- **ARICH Ntuple**: object used for debugging and code development, contains photon hits needed to calculate the Cherenkov angle.

and processing modules:

- **ARICH Unpacker**: unpacks the raw data from the ARICH sub-system data acquisition system (DAQ).
- **ARICH Packer**: used to pack simulated data and test if ARICH Unpacker works as its supposed to.
- **ARICH Reconstructor**: module used to fill ARICH Ntuple object. The module takes the track from Belle II tracking system and extrapolates the

track of the charged particle to ARICH photon detector plane. The module computes the entire particle likelihood function needed in particle identification.

- **ARICH DQM**: module is used to produce data quality plots to see how ARICH sub-system performs.
- **ARICH Btest**: module is used to process test beam data.
- **ARICH Background**: is used to estimate the effects of the background radiation on measurements of ARICH sub-system.

The Belle II experiment has a general data production group that processes all of the data produced by Belle II spectrometer sub-systems. For ARICH the processing chain that is used in general Belle II processing is described in Figure 4.2.

ARICH part of the processing chain produces and stores all the relevant ARICH data into calibration data files named `cdst.root`. `cdst.root` files contain raw and processed data from all sub-systems. They can be re-used when we want to reprocess only the data from specific sub-system. `cdst` files are useful when we perform studies that involve code changes only on the level of ARICH sub-system.

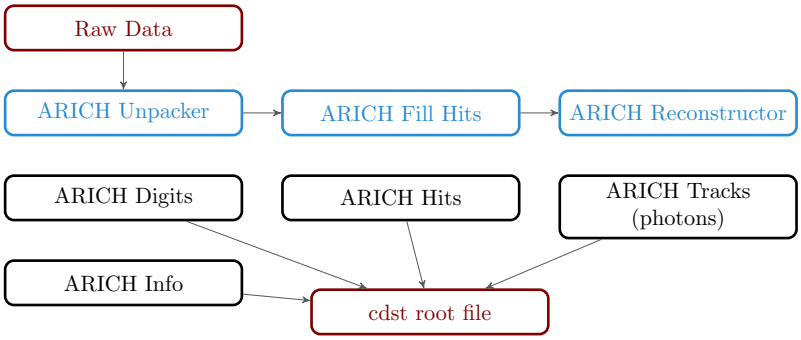

Figure 4.2: Production of ARICH data in general Belle II processing scheme.

For calibration purposes the another independent processing chain was used:

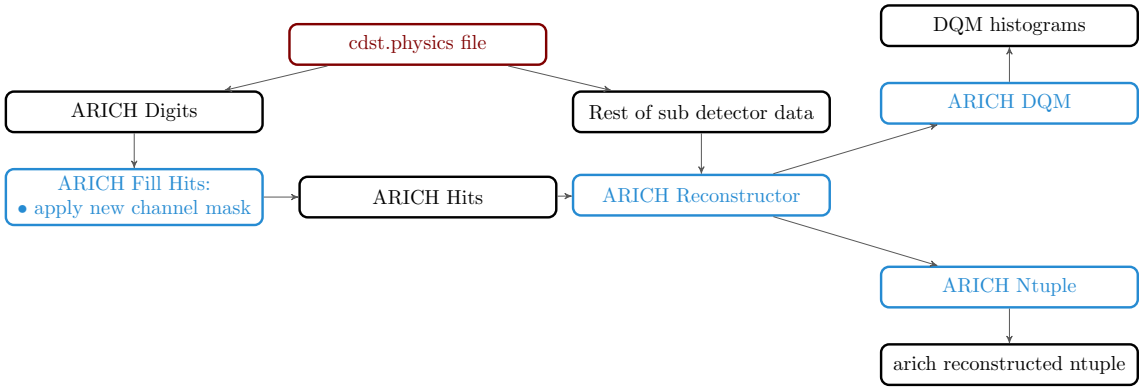

Figure 4.3: ARICH calibration processing chain.

Processing chain used in calibration process (See Figure 4.3) uses `cdst.root` files to obtain all of the tracking information and allows us to reprocess only the raw

data provided by ARICH sub-system. This approach reduces the complexity of our code tremendously and saves us a lot of computing time since we need to re-run only the ARICH part of the software in our studies.

4.3 Cherenkov distribution model

To determine wether our calibration was successful we want to check if there had been a reduction of background in the Cherenkov distribution. In order to determine amount of signal and background we perform the signal-background separation using the model of two Gaussians:

$$g_s(x) = ae^{-\frac{(x-\theta_{c_1})^2}{\sigma_1^2}} + be^{-\frac{(x-\theta_{c_2})^2}{\sigma_2^2}}.$$

The combination of two Gaussians is used to describe the presence of two populations. One Gaussian describes the Cherenkov distribution for population of clean events and the other Gaussian represents the population of events that are correlated to the background.

Background photons can be produced by charged particles from beam background; by photons whose path is slightly changed due to Rayleigh scattering; damaged electronics; or photon detector electronic components with wrong settings. The uncorrelated background photons are uniformly distributed over the detector area and their number linearly increases in range $\theta_c \in [0.1, 0.5]$:

$$g_b(x) = cx + d \quad x \in [0.1, 0.5]$$

From $\theta_c \approx 0.5$ the background starts to linearly decrease since the photon detector plane covers only a portion of the phase space.

The entire model for Cherenkov distribution:

$$g(x) = g_s(x) + g_b(x) \tag{4.1}$$

where $g_s(x)$ represents the signal model and $g_b(x)$ the background model. Parameters $a, b, c, d, \theta_{c_1}, \theta_{c_2}, \sigma_1, \sigma_2$ are obtained from fitting the model to the measured Cherenkov distribution.

If we now perform a fit on normalised Cherenkov distribution in range $[0.1, 0.5]$ we can then use the fit parameters to calculate the amount of signal N_s and background N_b we have in the region around mean Cherenkov angle $\theta_c \approx 0.3$. The area we integrate is defined by $\theta_{c_{min}} = \theta_{mean} - \sigma_{\theta_c}$ and $\theta_{c_{max}} = \theta_{mean} + \sigma_{\theta_c}$ (See Figure 4.4). The integrals $\langle N_s \rangle, \langle N_b \rangle$ are defined via:

$$\langle N_s \rangle = \int_{\theta_{c_{min}}}^{\theta_{c_{max}}} g_s(x)dx \tag{4.2}$$

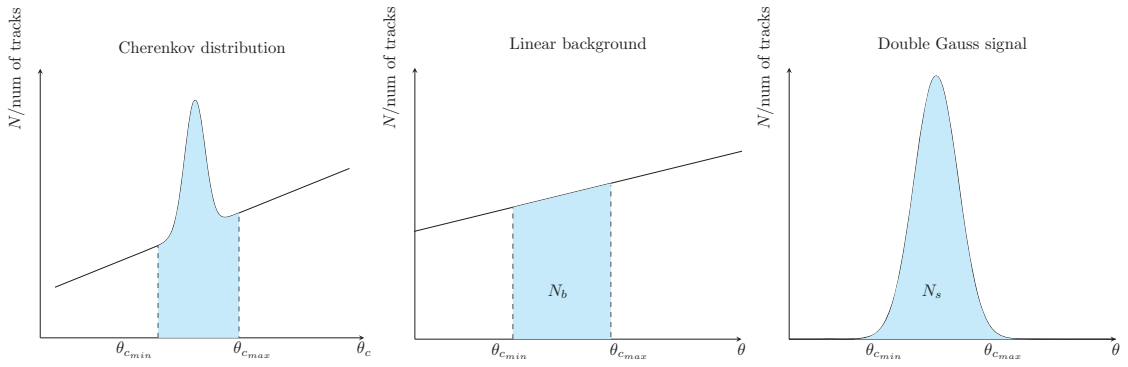

Figure 4.4: Left: Full Cherenkov distribution. Middle: Background distribution. Right: Signal distribution.

$$\langle N_b \rangle = \int_{\theta_{c_{min}}}^{\theta_{cmax}} g_b(x)dx \tag{4.3}$$

We also tested the model of a single Gauss with linear background and a double Gauss with the background of the second-order polynomial. But it turns out the model of double Gauss and linear background is the most appropriate one and accurately describes the physics behind photon sources that form the full measured Cherenkov distribution.

4.4 Signal-background ratio improvment

The goal of our work is to reduce the background in the measured Cherenkov distribution. So to quantify the signal improvement due to the background removal we introduce the signal to the background ratio:

$$SB = \frac{\langle N_s \rangle}{\langle N_b \rangle},$$

and the quantity that determines wether we improved the signal to the background ratio with removal of the background:

$$\text{SB}_{\text{ improvement}} = \text{SB}_{\text{ after cut}} - \text{SB}_{\text{ before cut}}.$$

The cut indicates that we changed a specific parameter in our ARICH sub-system data processing to remove particular photons. In the upcoming analysis, we use two types of calibration cuts:

- the number that determines when a specific channel is hot and,
- the maximum number of hits per APD module that still represent Cherenkov photons.

4.4.1 Background model

By performing cuts on our data, we will remove a certain amount of photons. But we need to be careful so our cuts do not remove the photons that represent the signal. When we cut the signal photons our background will not be linear (see Figure 4.5 left) any more but will contain a small Gaussian bump (see Figure 4.5 right).

We want to distinguish programmatically between the removed background that was linear and the removed background that had a Gaussian bump. To make the distinction, we perform a linear fit on the removed background for a specific cut in the range $\theta_c \in [0.1, 0.5]$. To determine whether the fit model and the distribution match we use a χ^2 test.

To confirm with 99% confidence that the model with p paremeters and distribution in N bins match we need the value of χ^2 for $N - p - 1$ degrees of freedom:

$$\chi^2_{correct} = \chi^2_{>99\%}(N - p - 1)$$

where $\chi_{>99\%}$ is obtained from the lookup tables.

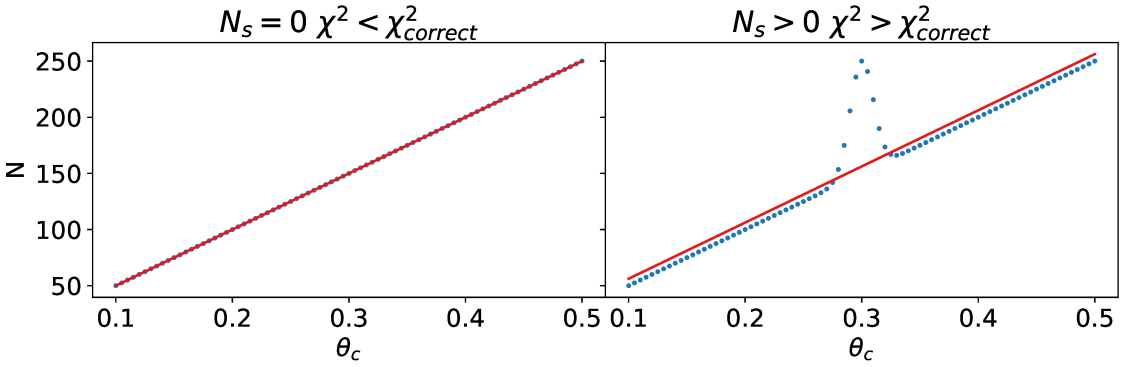

Figure 4.5: Left: Background that contains no signal photons. Right Background that contains signal photons.

Chapter 5

Results

In this chapter, we present the findings we came across during the calibration analysis.

5.1 Identification of hot channels

First, we identify the channels that detect photons too often (hot channels) for a single run `2018-exp3-01869`.

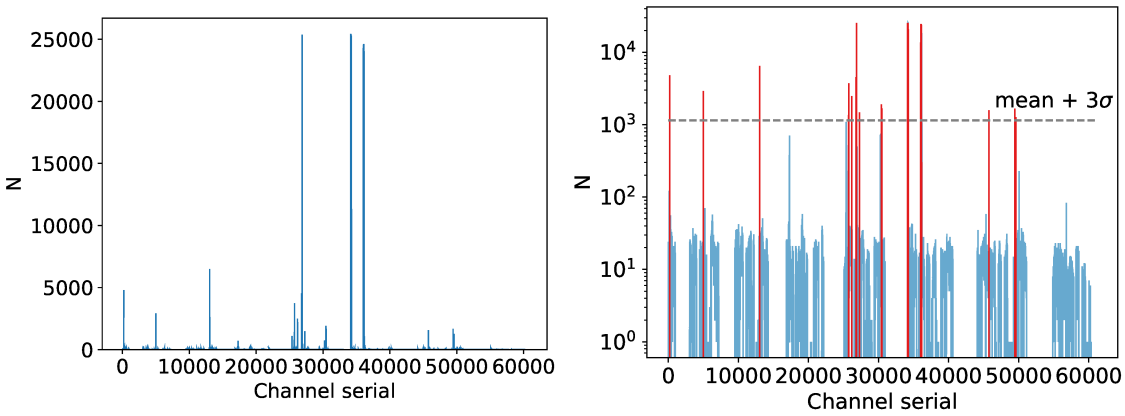

Figure 5.1: Run `2018-exp3-01869`. Left: number of hits per channel. Right: Hot channels that have more than mean $+ 3\sigma$ hits are marked red.

We start by counting how many photon hits did each ARICH channel have in the run `2018-exp3-01869`. We obtain a histogram Figure 5.1 left. We can see that certain channels recorded way more photon hits than others.

We determine what channels are hot by computing the average number of hits per channel (mean) and the corresponding variance σ. Channel is hot if the number of hits in that channel exceeds:

$$\text{hot channel threshold} = \text{mean} + 3\sigma.$$

If we mark hot channels Figure 5.1 right we see that certain channels exceed the threshold of mean + 3σ. We declare them as hot.

To see the influence of the hot channel threshold on the Cherenkov distribution we check how the Cherenkov angle distribution changes once we remove photon hits from the hot channels.

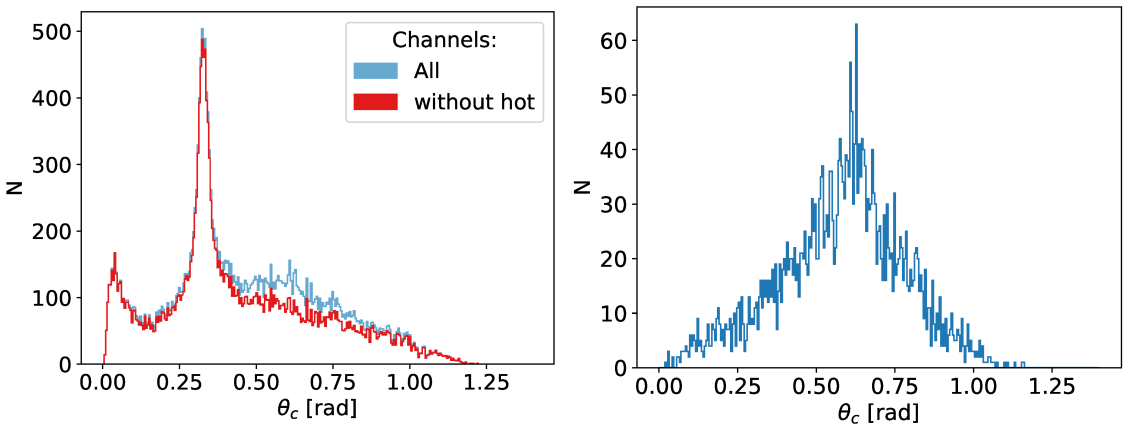

Figure 5.2: Left: Comparison of Cherenkov distribution for all photon hits and distribution without hits in the hot channels. Right: Difference between Cherenkov distribution with all hits and distribution without hits from hot channels.

First, we plot a Cherenkov distribution where we take into account all photons Figure 5.2 left (blue distribution). Then we plot a Cherenkov distribution where we removed hits from the hot channels Figure 5.2 left (red distribution). We see a small difference. If we now subtract the Cherenkov distribution without hot channels from the full one, we obtain a background distribution Figure 5.2 right.

From Figure 5.2 right we see that the background increases as expected linearly up to $\theta_c \approx 0.60$ rad and then falls back to zero. The background has no Gaussian bumps so we can conclude that we did not cut out any signal.

Naively we could finish our work here but further investigation reveals that the hot channel threshold defined with mean and σ is not a proper metric for hot channel determination. In specific runs we happen to cut a proportion of the signal with mean + 3σ threshold for hot channels. To get a better estimate of the hot channel threshold we look into channel occupancies.

5.1.1 Channel occupancy

To quantify the amount of signal in each channel we introduce the quantity of channel occupancy as:

$$\text{ch. occupancy} = \frac{\text{number of hits per channel per run}}{\text{num of events per run}} \tag{5.1}$$

ch. occupancy tells us how often a specific detector channel was hit. Did the channel have a lot of hits or a small amount of hits in a specific run?

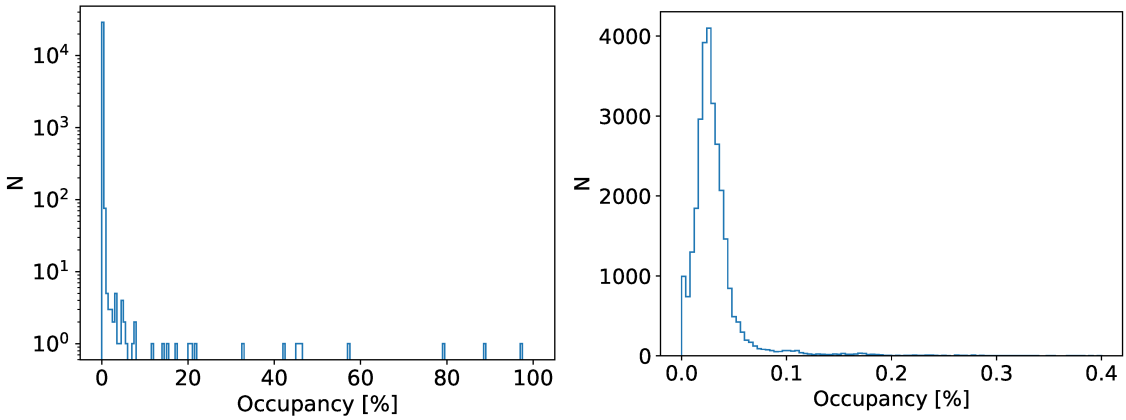

Figure 5.3: For run `2018-exp3-02475`. Left: occupancy distribution. Right: occupancy distribution in range $[0, 0.4]\%$

We want to know how many of the detector channels in the specific run had a small number of hits or a large number of hits. If we plot occupancies into a histogram, we obtain Figure 5.3 left or the occupancy distribution. From the occupancy distribution we see that a few channels have a large number of hits but the majority of the channels had few hits per run. If we look at Figure 5.3 right we could wrongly assume that any channel that has occupancy above 0.2% is hot.

It turns out that for every run from 2018, experiment 3 and from 2019 experiment 7 the occupancy distribution as defined in Figure 5.3 is slightly different. To determine how different the occupancy distributions are we want to compare these distributions for all measurement runs from experiment 3 and 7.

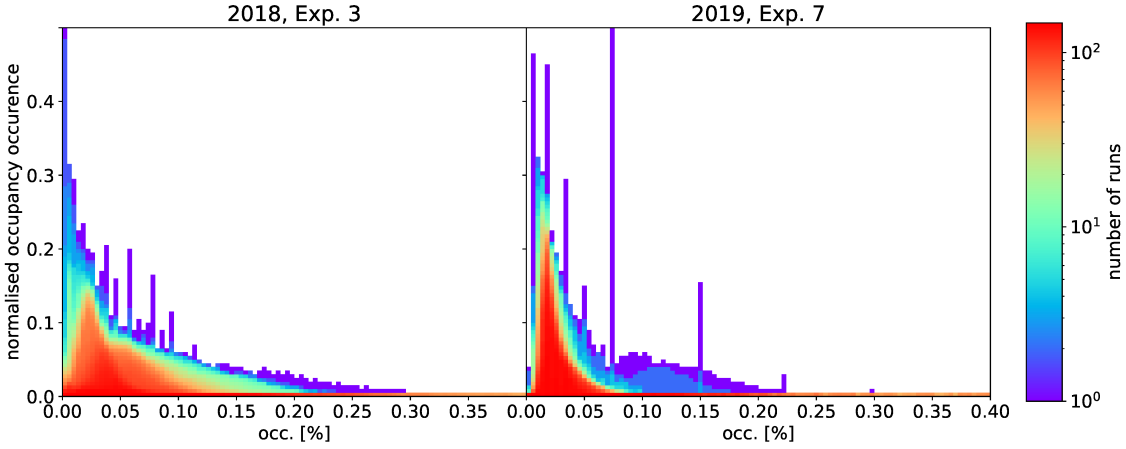

Figure 5.4: Comparison of occupancy distributions for all runs from: 2018, experiment 3 (left) and 2019, experiment 7 (right).

To compare occupancy distributions for different runs we normalise each occupancy distribution with the number of active channels in that run. If we now compare oc-

cupancy distributions for every run from experiment 3 in 2018 and from experiment 7 in 2019 we obtain Figure 5.4. Colours in the plot tell us how often occupancy distributions overlap one another.

Occupancy distribution overlaps allow us to see that the red part is characteristic for most of the runs while we see slight differences in occupancy distributions from one run to another. Another thing we observe from Figure 5.4 is that channel occupancies for data from 2019 are smaller on average than channel occupancies in 2018.

There are several things that caused the differences in occupancy distributions. We need to know that during the operation of ARICH sub-system in 2018 different parts of the detector were turned on and off. Due to cooling problems only a half of ARICH sub-system photodetector plane was turned on at any moment. In 2019 however the entire ARICH sub-system was operational.

Another contribution to the differences in run occupancy distributions can be attributed to the fact that every run has a different amount of events per run. It's also worth mentioning that the particles produced by electron-positron collisions differ from event to event. Thus the type of physics processes we measured vary slightly from one run to another.

At each run different ARICH electronic components misbehave. They have to be recalibrated via software reloads or bias voltage changes. Each such change can influence the occupancy distributions we obtain for every run.

Despite all the effects that can cause changes to the occupancy distributions between different runs, we still want to know when the specific channel is hot. We define max. channel occupancy that allows us to distinguish between the hot channel and channel that behaved properly. Every channel that has an occupancy higher than the defined max. channel occupancy is hot.

From Figure 5.4, we see that any max. channel occupancy above 0.4% should be high enough that we do not remove any signal. But to confirm this assumption, we should take a closer look into the shape of the background attributed to the hot channels as a function of max. channel occupancy we chose.

5.1.2 χ^2 measure

If we now compute the background that was removed by setting max. channel occupancy to 0.4% we obtain a background distribution. Then we fit the obtained background distribution with the background model described in section 4.5. We then compute the χ^2 of the fit for obtained background distribution. If we repeat the process for every max. occupancy in range $[0, 1.0]$ in steps of 0.01 for run `2018-exp3-02475` and `2018-exp3-02476` we obtain value of χ^2 as function of max. occupancy.

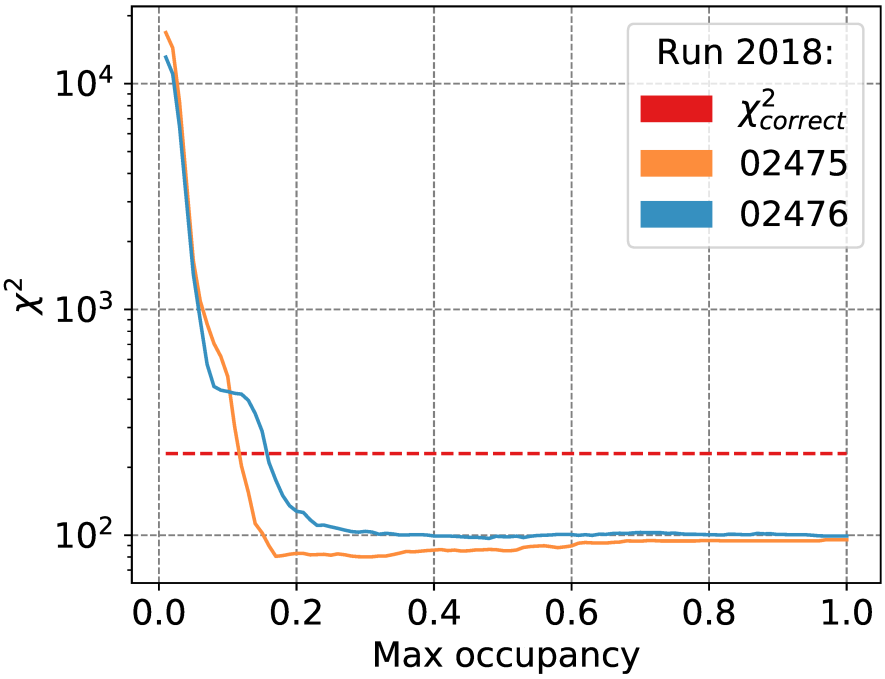

Figure 5.5: χ^2 of removed background vs. maximum channel occupancy for runs `2018-exp3-02475` and `2018-exp3-02476`.

From Figure 5.5 we can see that up to the max. occupancy of $\approx 0.15\%$ χ^2 for both runs backgrounds converge below $\chi^2_{correct}$. In other words from max. occupancy $\approx 0.15\%$ onwards backgrounds for runs `2018-exp3-02475` and `2018-exp3-02476` do not contain any signal any more.

Unfortunately, it turns out we have few hundred more runs to analyse. In some of the runs the signal was present in the background we removed at higher max. occupancies than 0.15%. After careful study we settled on the max. occupancy of 0.45% for experiment 3, 2018 data and 1.0% for experiment 7,2019 data as a measure between hot and normal working channel.

We compute for all the runs from 2018, experiment 3 and runs from 2019, experiment 7 the value of χ^2 of linear model background fit to the obtained background distribution. We observe that in most runs $\chi^2 < \chi^2_{correct}$(see Figure 5.6).

In runs where $\chi^2 > \chi^2_{correct}$ we would expect signal in the background distribution. But cases where $\chi^2 > \chi^2_{correct}$ are either a consequence of low statistics or the fact that background in those runs is not completely linear. However, none of the backgrounds where $\chi^2 > \chi^2_{correct}$ contains the signal for runs:

- from 2018, experiment 3 at occupancy cut of 0.45%,
- from 2019, experiment 7 at occupancy cut of 1.0%.

Kolmogorov-Smirnov test has a similar problem as the χ^2 test. Unfortunately, we

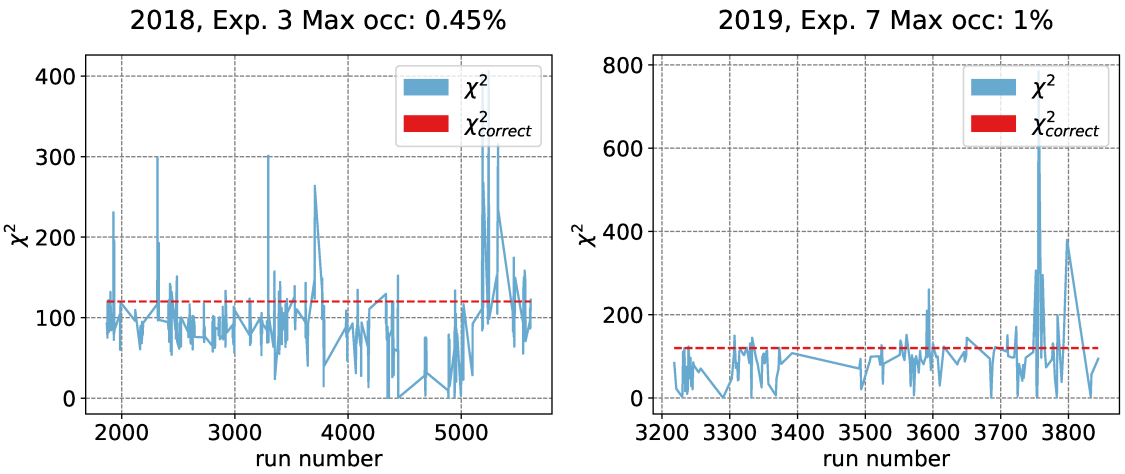

Figure 5.6: Value of χ^2 for the linear background obtained at max. occupancy 0.45% vs. run number for experiment 3 (left) and experiment 7 runs max. occupancy 1.0% (right).

can not use χ^2 or any other statistic to determine if the signal was present in the background we removed. Data of the runs changes too much over time. It turns out that we can not rely on a single number to tell us if any signal was removed. Instead, we use an alternative approach.

5.1.3 Sum of removed background

Another method to confirm there is no signal in the background we have removed is, to sum up all background distributions from all the experiment 3 runs (see Figure 5.7). We observe that the distribution has no bump around $\theta_c \approx 0.3$ and we are not removing any signal with max. occupancy cut of 0.45%.

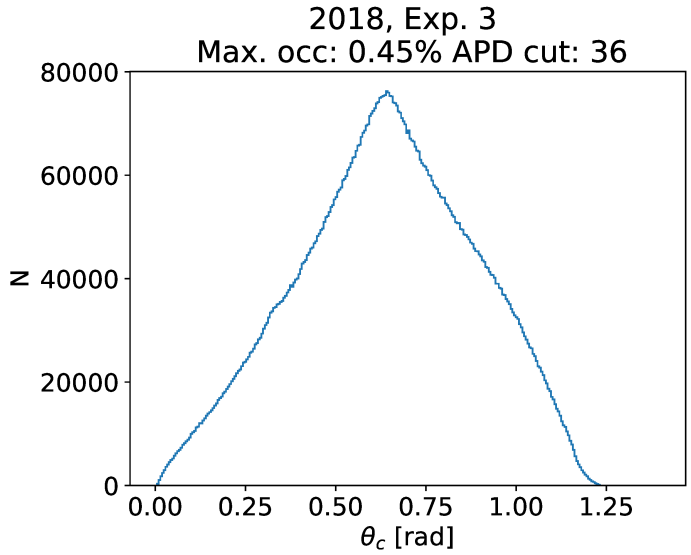

Figure 5.7: Background removed from all the runs from experiment 3 via occupancy cut of 0.45%.

However, for the experiment 7 runs we observe that we continue to cut out the signal at occupancy 0.45% (see Figure 5.8 left). If we shift the occupancy boundary for hot channel identification to 1%, we see a slight drop in the signal that our background contains (see Figure 5.8 right). But the signal peak is still there even at higher occupancies up to 2%. So we settle on maximum channel occupancy of 1%. It is a trade-off. We remove most of the background and a bit of signal.

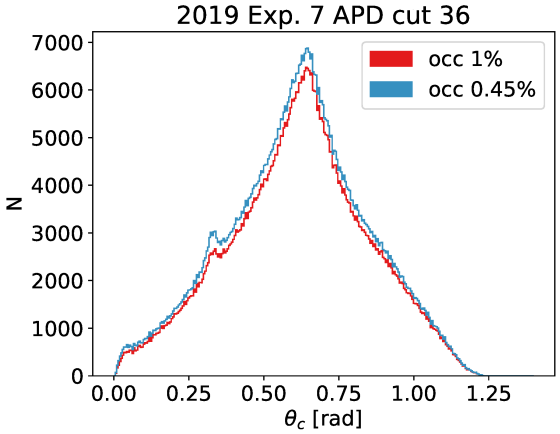

Figure 5.8: Hot channel background removed from the experiment 7 runs at max. occupancy 0.45% (blue) and 1% (red)

5.1.4 S/B ratio change

Next, we need to confirm that the signal to background ratio improved due to the removal of hot channels. We observe that for most of the runs, the signal to background ratio improves (see Figure 5.9). In cases where we do not see an improvement the runs had a small number of events.

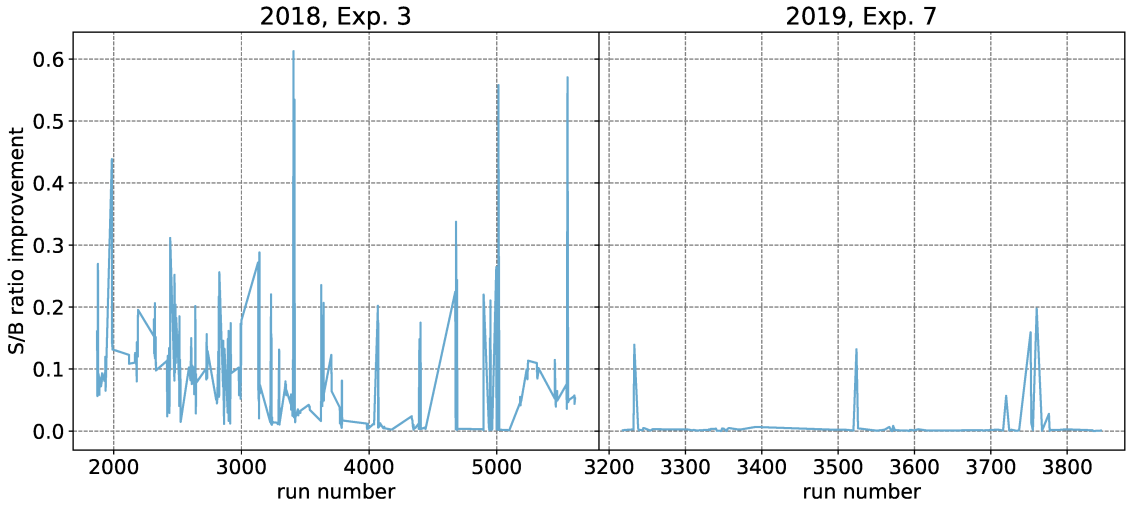

Figure 5.9: Improvement of signal to background ratio for the experiment 3 (left) and the experiment 7 (right).

5.1.5 Hot channels 2018/2019

With a max. occupancy of 0.45% for 2018 and 1% for 2019, we identify a different number of hot channels in each run (See Figure 5.10). In the experiment 7 we found significantly less hot channels even though the full ARICH HAPD plane was operational compared to experiment 3.

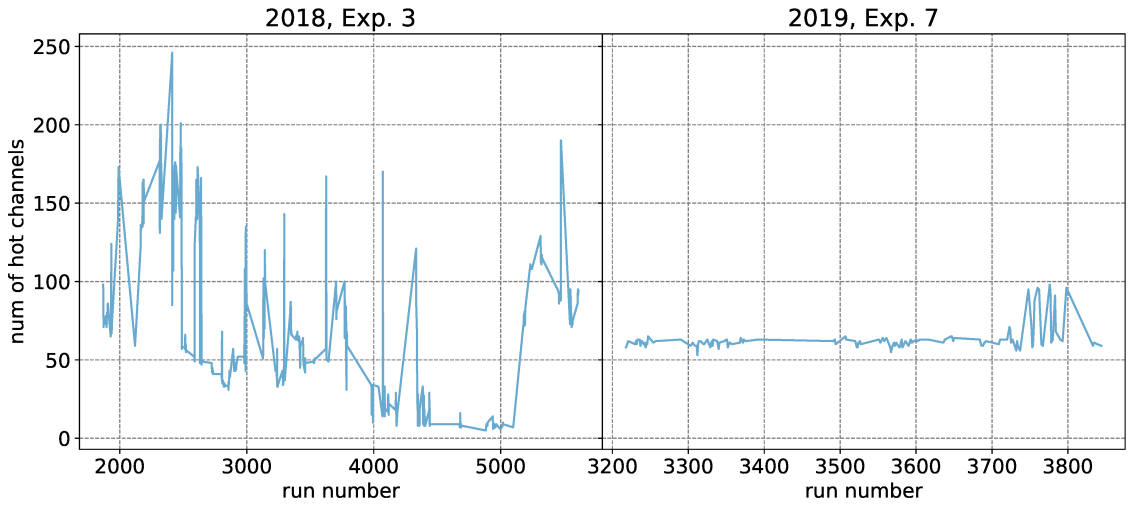

Figure 5.10: Number of hot channels at max. occupancy 0.45% for the experiment 3 (left) and at max. occupancy 1.0% for the experiment 7 (right).

5.2 HAPD flash events

Next to be analysed is the number of hits per APD/HAPD. If we look at an example of a Cherenkov ring on the ARICH HAPD detector plane (See Figure 5.11), we see that only a few pixels per each HAPD are hit.

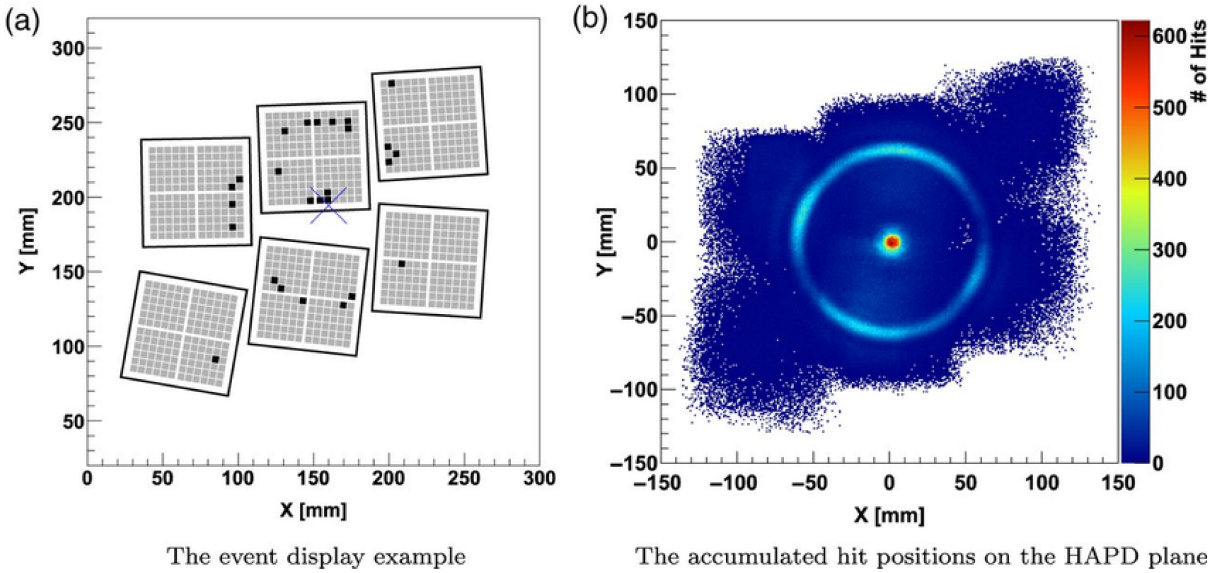

Figure 5.11: Left: Example of the Cherenkov ring at the HAPD plane. Right: Accumulated hit positions on the HAPD plane for multiple Cherenkov rings [1].

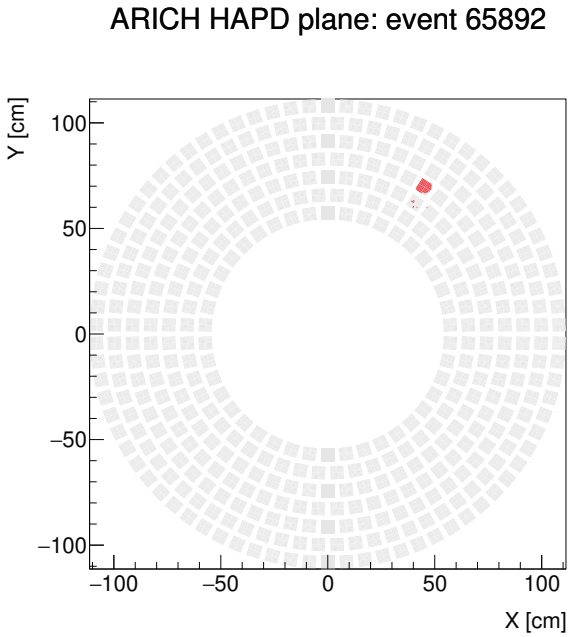

Figure 5.12: Example of a flash event where all pixels on the HAPD module detected a photon.

However, from time to time events like the one in Figure 5.12 occur. We observe that the entire HAPD or APD module glows. The only explanation why such an event would be detected is that the module malfunctioned.

Charged particles produce only a few photons per track. Those photons land on the area of several APD modules. Since there are only a few charged particles produced per e^+e^- collision, there's no reason why all of the 36 APD pixels could be hit. We want to determine how many hits per APD could still be produced by Cherenkov rings and in which case there was a detector malfunction.

We want to check how many hits per HAPD/APD we have. By creating a histogram where we count how many hits per APD in an event we had we obtain Figure 5.13 left. From Figure 5.13 left we see that in some cases all 36 APD pixels were hit. By looking at the histogram for the number of hits per HAPD per event we observe a similar effect - Figure 5.13 right. There are cases where all channels of the HAPD chip are hit which has to be a consequence of the detector malfunction.

Next, we want to check if the number of hits per APD per event is somehow connected to the number of hits per HAPD per event. To check for any correlations, we create a two-dimensional histogram that has a number of HAPD hits per event on x-axis and number of APD hits on the y-axis.

Once we fill the two-dimensional histogram, we obtain Figure 5.14. We observe that slight correlation is present between the number of hits per APD and number of hits per the corresponding HAPD. We observe that we have two types of events.

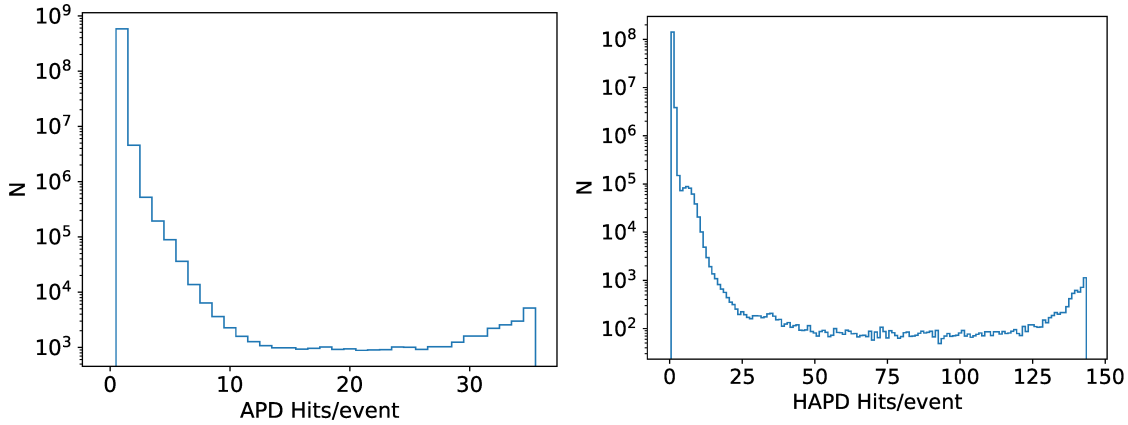

Figure 5.13: Left: number of APD hits per event. Right: number of HAPD hits per event.

First type are events where we have a low number of hits per APD/HAPD and the second type are events where we have a high number of hits per APD/HAPD. There are not many events that would have a medium number of hits per APD/HAPD.

Due to the slight correlation between the number of hits per APD and HAPD per event we only check how limiting the maximum number of hits per APD influences the Cherenkov distribution. We introduce a second cut: APD cut or a maximum number of hits per APD we except as reasonable for Cherenkov rings.

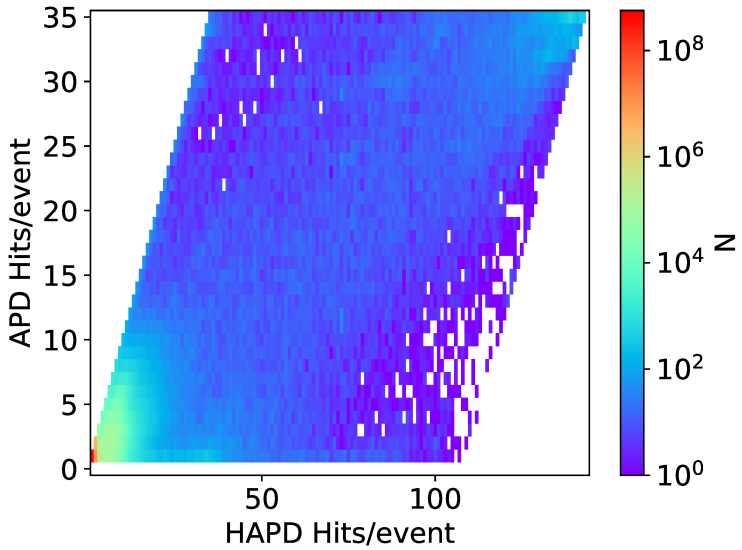

Figure 5.14: Number of hits per HAPD/event vs. number of hits per APD/event.

5.2.1 Cherenkov distribution

To determine how many hits per APD module are expected for Cherenkov rings formed by charged particles, we visualise the Cherenkov distribution vs the maximum number of hits per APD per event. We stipulate that in a specific event the

APD module with the most hits had 20 photon hits. We plot Cherenkov angles of all photons in that event into the row where the number of hits per APD is 20.

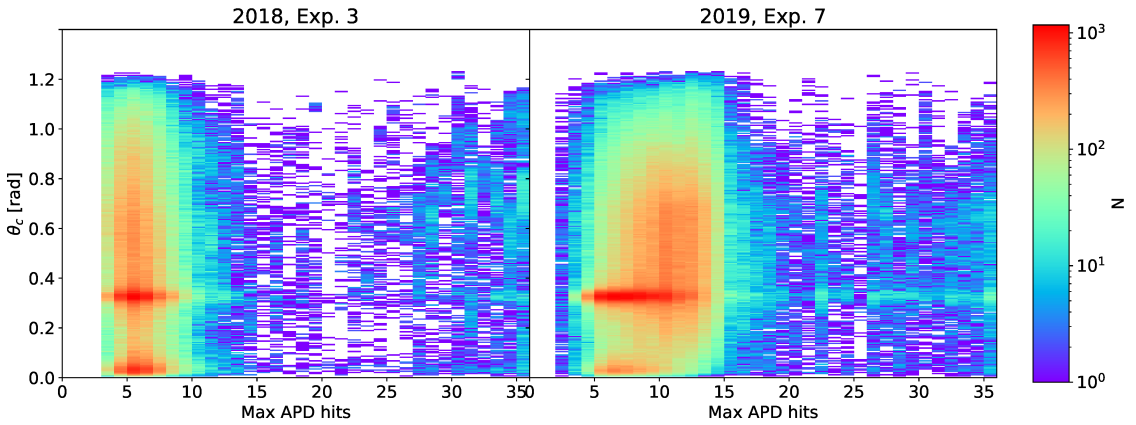

Figure 5.15: Cherenkov angle distribution vs. maximum number of APD hits per APD for the experiment 3 (left) and the experiment 7 (right).

From Figure 5.15 we can see that the Cherenkov distribution stretches up to a certain amount of hits per APD. In case of the experiment 3 that's up to 12 hits per APD and for the experiment 7 up to 16 hits per APD. We want to know what kind of background we remove by removing the APD modules that had more than 16 photon hits per APD. To remove APD flash events we remove all APD-s that had more than 16 photon hits per APD.

5.2.2 Removed background

To confirm that we did not cut any signal we sum up all the backgrounds obtained for the experiments 3 and 7. From Figure 5.16 we can see that the signal is not present in the distribution of photons that we proclaimed as background.

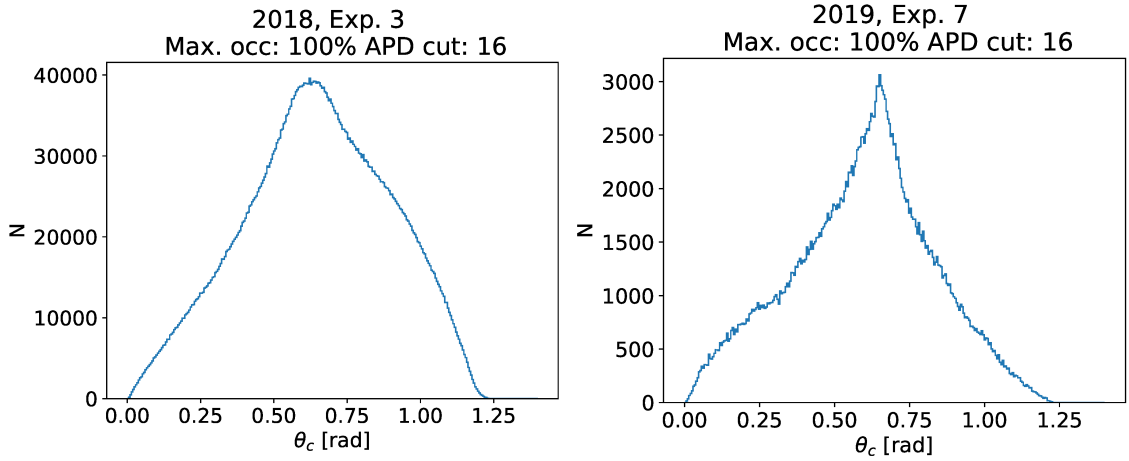

Figure 5.16: Background removed with APD 16 cut for the experiment 3 (left) and the experiment 7 (right).

5.2.3 S/B ration change

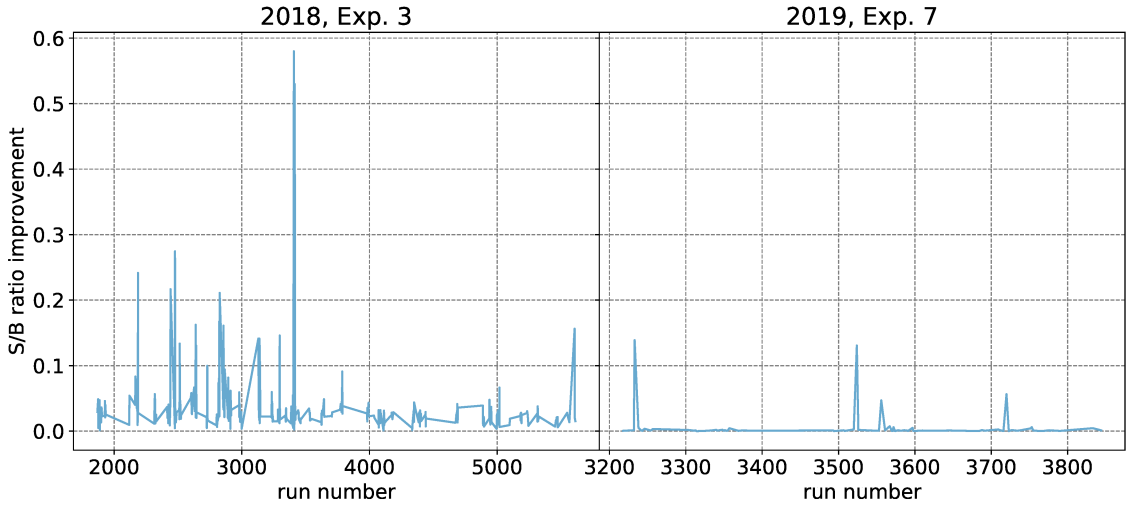

Figure 5.17: Signal to noise ratio improvement due to APD 16 cut for the experiment 3 (left) and the experiment 7 (right).

If we compute the signal to background ratio improvement, we see from Figure 5.17 that for both data sets from 2018 and from 2019 the ratio improves. In the cases of runs where the ratio does not improve, we either had low statistics in the background or the background was non-linear but not due to signal present in the background.

5.3 Influence on μ^+, μ^-, e^+, e^- events

So far we have analysed the effects of the removal of hot channels and APD flashes on the full population of charged particles. We now look at the Cherenkov distribution of Bhabha $e^+e^- \to e^+e^-$ scattering and di-muon $e^+e^- \to \mu^+\mu^-$ scattering events.

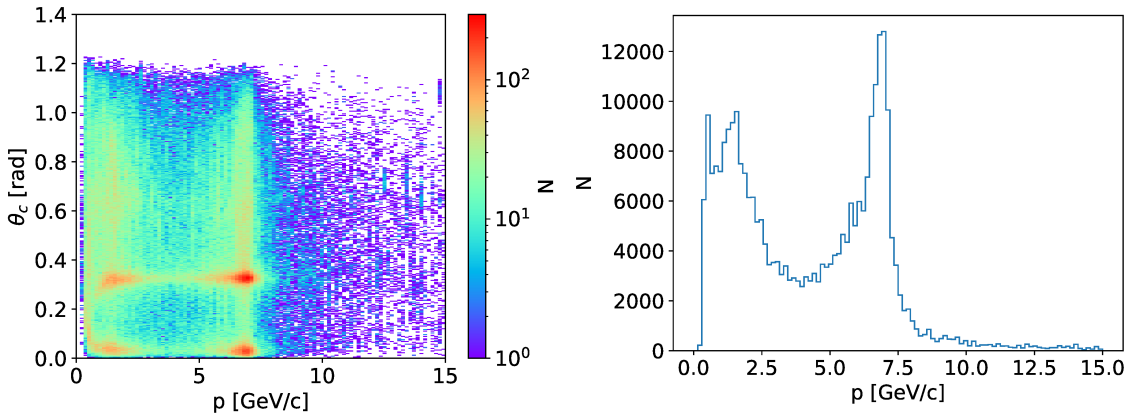

Figure 5.18: Run `2018-exp3-02475` Left: Cherenkov angle distribution vs. momentum. Right: momentum distribution for charged particles that fly through ARICH sub-system.

5.3.1 Bhabha $e^+e^- \to e^+e^-$ scattering

When an electron and a positron collide they can produce a new pair of an electron and a positron. Such a process is called Bhabha scattering.

If we plot Cherenkov distribution vs the momentum of charged particles we see from Figure 5.18 left that we have a majority of Cherenkov photons at momentums of 1 GeV/c and 6 GeV/c. The distribution at 6 GeV/c are photons produced by Bhabha scattering. We now look only at the Bhabha events. To obtain Bhabha Cherenkov distribution, we make the selection of photon hits that were produced by charged particles with $p > 6$ GeV/c.

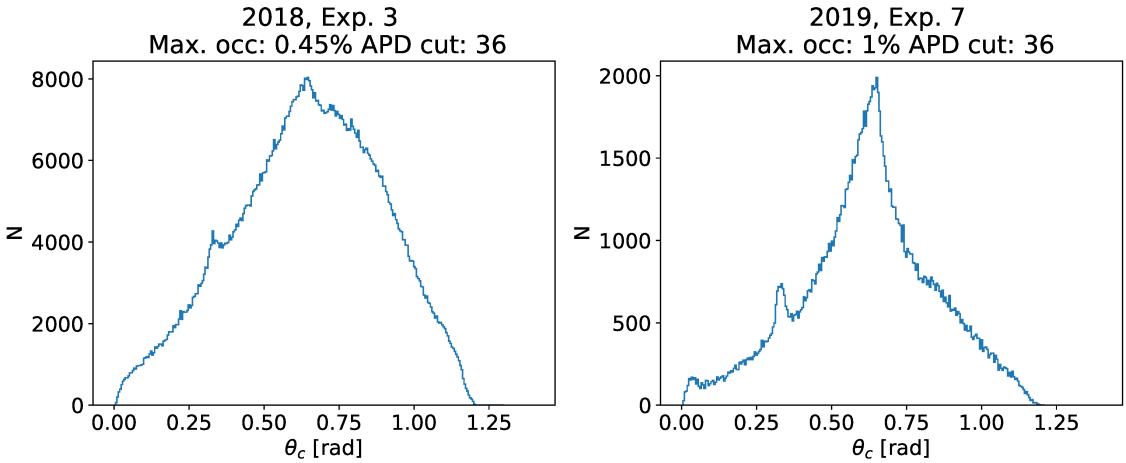

Figure 5.19: Removed background due to hot channels for the Bhabha events in the experiment 3 (left) and the experiment 7 (right).

In Figure 5.19, we can see the effect of maximum occupancy cut for the Bhabha events. We observe that for the experiment 7, we have removed a bit of a signal. The result is not surprising since this has been observed already when analysing the selection of all events.

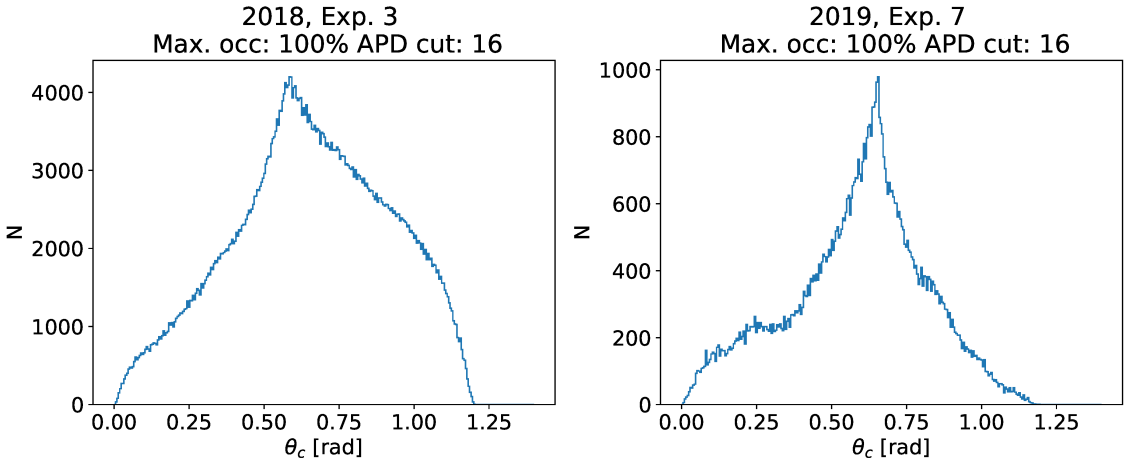

Figure 5.20: Removed background due to APD flashes for the Bhabha events in the experiment 3 (left) and the experiment 7 (right).

In Figure 5.20, we observe the effect of the max number of hits per APD cut on the Bhabha events. We are not cutting any signal in this case for any of the runs in 2018, 2019.

5.3.2 Di-muon μ^+, μ^- events

To select the events where the electron-positron collision produced two muons is slightly harder. So we use the data samples prepared by the Belle II data processing group, where the event was $e^+e^- \to \mu^+\mu^-$.

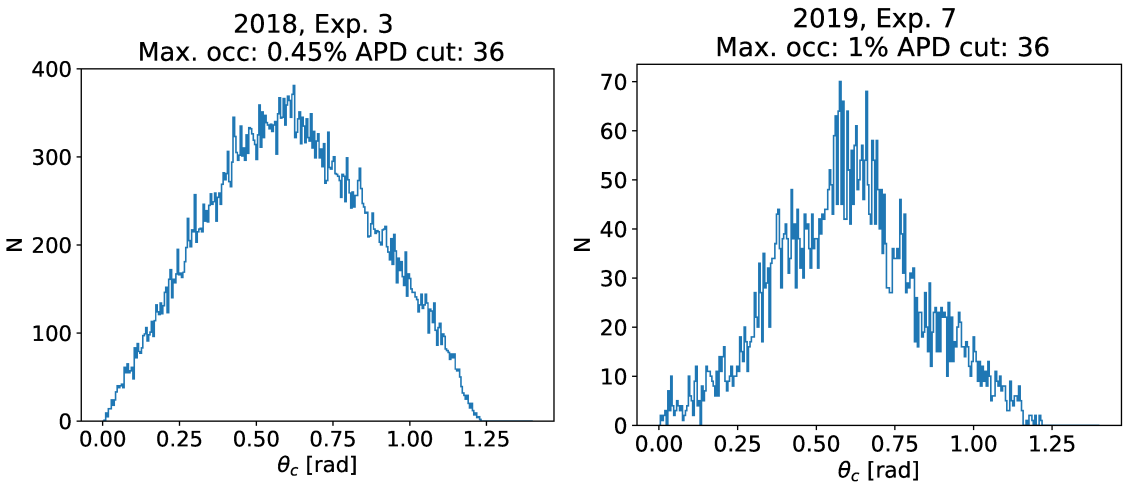

Figure 5.21: Removed background due to the hot channels for di-muon events in the experiment 3 (left) and the experiment 7 (right).

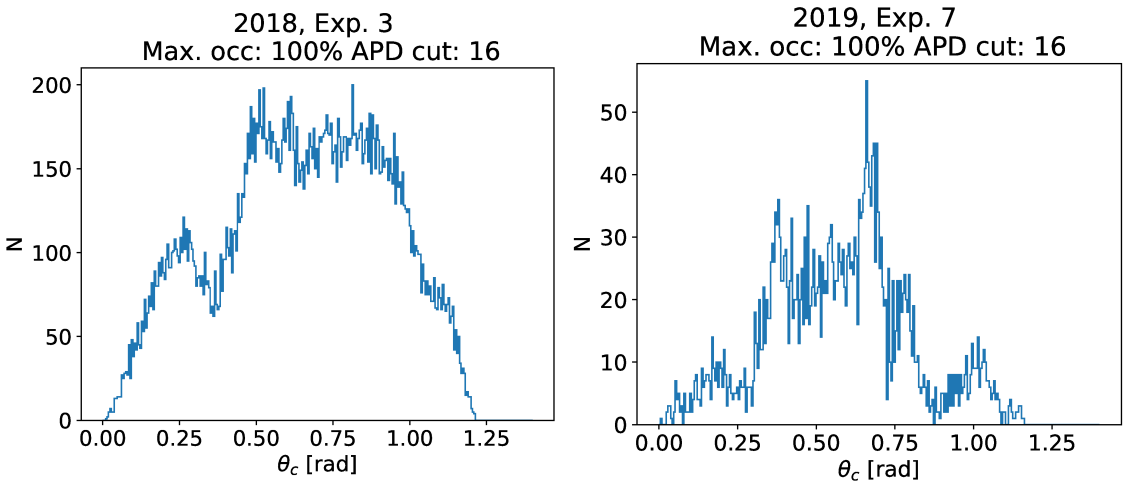

Figure 5.22: Removed background due to APD flashes for di-muon events in the experiment 3 (left) and the experiment 7 (right).

From Figure 5.21 we see that the background we have removed with the hot channel cut for di-muon events contains no signal.

However, the background we have removed with APD cut is non-linear and not at all what we would expect (see Figure 5.22). The non-linearity of the distribution on figure 5.22 is most probably due to the low statistics but we can not claim that for sure.

Chapter 6

Conclusion

This thesis provides several results useful for ARICH sub-system calibration process:

- The best model for Cherenkov distribution is a combination of two Gaussian functions and a linear function.
- To remove the hot channels we need to cut all the channels that have occupancy above:
  - 0.45% for 2018, the experiment 3 and,
  - 1.0% for 2019, the experiment 7 measurement campaigns.
- To remove APD flash events we need to cut all APD modules where the number of detected photons per APD exceeded 16 photons.
- Summation of background distributions from all runs for specific measurement campaigns is the simplest method that checks if our hot channel cut or APD cut have removed any signal.
- With proposed cuts we indeed improve the signal to noise ratio in the measured Cherenkov distributions.

We proposed a set of calibration parameters that can be used by ARICH sub-system group to improve sub-systems future operations. Obtaining above results required much patience, learning and overcoming several obstacles :

- Navigation of the Belle II collaboration bureaucracy.
- Setup of the Belle II computing environment with all the authentication certificates.
- Learning the ropes of `basf2` software framework that the Belle II collaboration uses for data processing.
- How `basf2` framework manages memory. How data is stored and passed around.
- How the ARICH sub-system software modules work. What type of data they produce and how.

- Learning how to use the `KEK` computing cluster in Japan for processing of large volumes of data.
- Learning the trade-offs between storing all processed data sets and storing a minimal amount of probability distributions needed for analysis.

Povzetek v slovenskem jeziku

7.1 Motivacija

Leta 2008 se je pričel razvoj spektrometra Belle II in trkalnika SuperKEKB. Trkalnik preko trkov elektronov in pozitronov proizvaja mezone B. Posamezni poddetektorji spektrometra Belle II nato izmerijo, kakšni delci so nastali ob razapdu mezonov B. Eden izmed poddetektorjev, ki določa identiteto nastalih nabitih delcev, je detektor obročev Čerenkova (ARICH). ARICH je sestavljen iz dveh slojev aerogela in sloja, ki vsebuje pozicijsko občutljiv fotonski detektor. Posamezne Čerenkove fotone, ki jih nabiti delci izsevajo, ko prečkajo aerogel, zaznajo kanali fotonskega detektorja.

Do začetka leta 2018 je bila večina komponent spektrometra končana in pričel se je proces kalibracije poddetektorjev. V času kalibracije je bilo opaženo, da določeni kanali ravnine fotonskega detektorja ARICH ne zaznavajo fotonov (mrtvi kanali) in da nekateri kanali zaznavajo fotone tudi v primeru, ko fotonov na kanalih ni bilo (vroči kanali).

Cilj te naloge je razvoj kalibracijskega postopka, ki omogoči identifikacijo napačno delujočih kanalov fotonskega detektorja.

7.2 Eksperiment Belle II

7.2.1 Fizikalni program

Spektrometer Belle II je del trkalnika SuperKEKB v Tsukubi na Japonskem. Trkalnik je zasnovan z namemon, da proizvede veliko število mezonov B. Tekom delovanja bo eksperiment Belle II zbral 50 krat več podatkov, kot jih je zbral njegov predhodnik Belle I. Velik vzorec izmerjenih mezonov B bo raziskovalcem omogočil:

- natančne meritve s področja fizike okusa,
- študije primerov, kjer je kršena nabojno-parna (CP) simetrija,
- meritve elementov CKM matrike,
- iskanje fizikalnih procesov, ki jih Standardni model ne popiše,
- natančne meritve redkih razpadov mezonov B, D in leptonov τ.

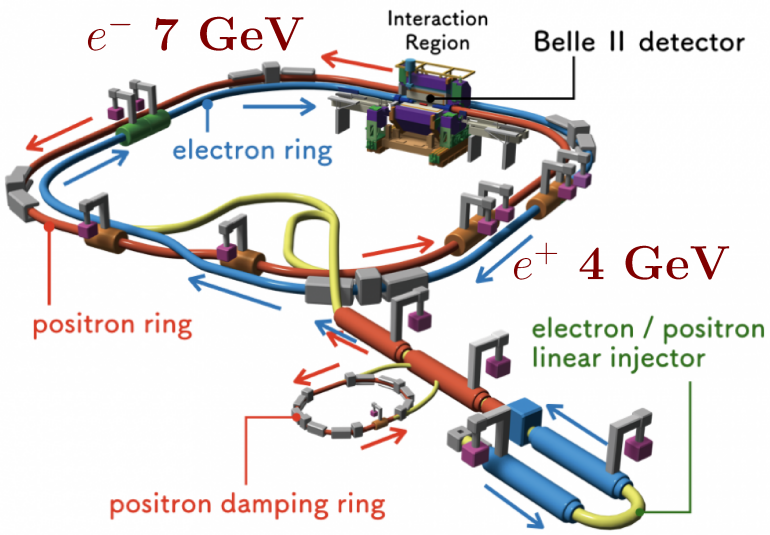

Slika 7.1: Skica trkalnika SuperKEKB in spektrometra Belle II [1].

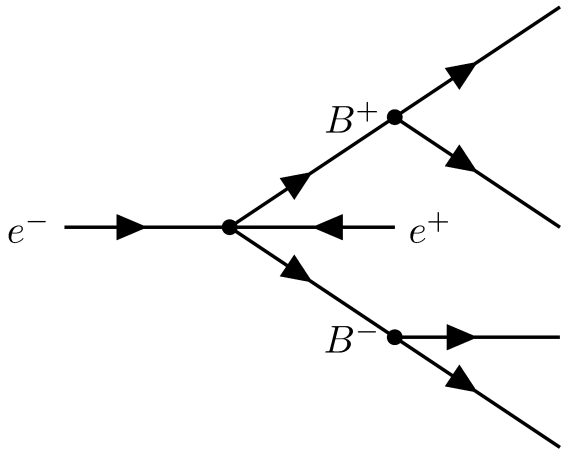

Slika 7.2: Primer anihilacije elektrona in pozitrona v par mezonov B, ki nato razpadeta.

7.2.2 Tovarna mezonov B

Spektrometer Belle II je del trkalnika elektronov in pozitronov SuperKEKB. Trkalnik je zgrajen dvanjast metrov pod zemljskim površjem in ima premer en kilometer. Podzemni del je sestavljen iz linearnega pospeševalnika in trkalnika (slika pospeševalnika 7.1).

Linerani pospeševalnik s pomočjo radio frekvenčnih votlin pospeši elektrone do energije 7 GeV in pozitrone do energije 4 GeV. Ko so delci pospešeni, vstopijo v obroč, po katerem krožijo, dokler jih v spektrometru Belle II ne trčimo. Za kroženje nabitih delcev po obroču poskrbijo dipolni magneti. Za ostrino curka elektronov in pozitronov poskrbi sistem kvadropolnih magnetov.

Ko curka pozitronov in elektrononov trčita, pride do anihilaicje pozitronov in elek-

tronov. Ob anihilaciji nastane kratkoživa nevtralno nabita mezonska resonanca, ki razpade na pare mezonov B.

Ker je energija žarka elektronov večja kot energija žarka protonov, se težišče sistema premakne v smeri curka elektronov. Premaknjenost težišča povzroči nesimetričen trk e^+ e^-. Nesimetričnost trka povzroči nastanek pospešenih mezonov B. Nastala mezona nato razpadeta v produkte, ki jih lahko zaznamo (mezoni, barioni, fermioni, fotoni) in produkte, ki jih ne moramo zaznati (nevtrnini in drugi nepoznani delci). Preko meritev končnih razpadnih produktov lahko rekonstruiramo fizikalni proces, ki se je zgodil. Trk elektrona in pozitrona imenujemo dogodek (primer dogodka slika 7.2).

7.2.3 Spektrometer Belle II

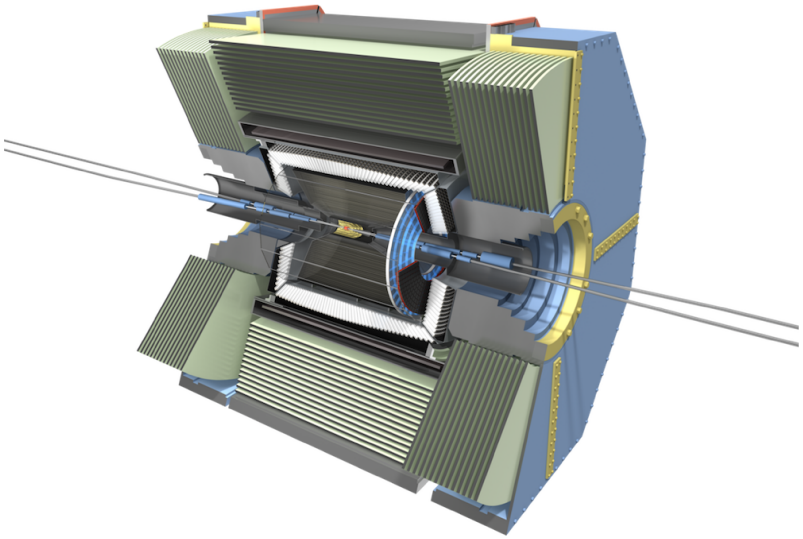

Slika 7.3: Spektrometer Belle II.

Naloga spektrometermetra Belle II (slika 7.3) je identifikacija delcev, ki so nastali ob trku elektronov in pozitronov. Spektrometer ima čebuli podobno strukturo. V centru se nahaja sistem za določanje gibalnih količin nabitih delcev. Gibalne količine so določene preko meritve ukrivljenosti trajektorij nabitih delcev v magnetnem polju $B = 1.5T$. Sledita dva detektorja za določanje identitete delcev preko Čerenkovega efekta. Zunanji sloj spektrometra sestavljajo elektromagnetni kalorimeter in mionske komore.

7.3 Detektor Čerenkovih obročev

7.3.1 Čerenkov efekt

Nabiti delec, ki potuje skozi material s hitrostjo v, večjo kot je hitrost svetlobe v mediju, povzroči Čerenkovo sevanje. Delec izseva fotone pod določenim kotom, ki ga imenujemo Čerenkov kot. Razdalja, ki jo prepotuje nabit delec v materialu vt

in razdalja, ki jo prepotuje izsevan foton ct tvorita pravokotni trikotnik (slika 7.4). Posledično lahko Čerenkov kot definiramo preko preproste trigonometrije kot:

$$\cos\theta_c = \frac{ct}{vt} = \frac{c_0}{vn} = \frac{1}{n\beta} \qquad \beta = \frac{v}{c_0}$$

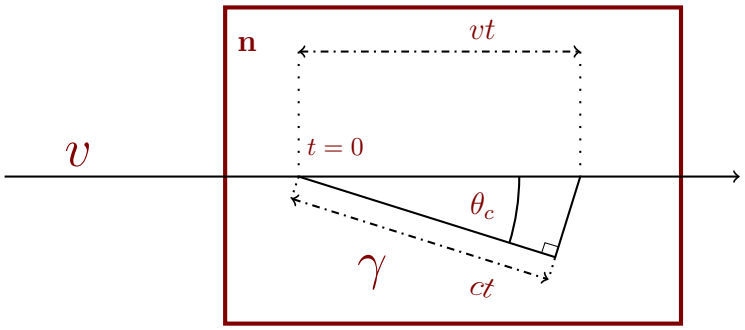

Slika 7.4: Shema poti nabitega delca, ki potuje skozi blok materiala (z lomnim količnikom n) in foton γ izzsevan pod Čerenkovim kotom θ_c.

Če poznamo Čerenkov kot in lomni količnik, lahko določimo hitrost nabitega delca. Za vsak nabit delec lahko ocenimo, koliko fotonov N bo izseval ob preletu materiala z enačbo povzeto po Jelly [6]:

$$N \approx d\left(1 - \frac{1}{n^2\beta^2}\right).$$

Število izsevanih fotonov je sorazmerno debelini d materiala, skozi katerega potuje nabit delec in faktorju, ki je odvisen od lomnega količnika in hitrosti nabitega delca. Število izsevanih fotonov za nabit delec je majhno.

Napaka pri meritvi Čerenkovega kota je definirana preko enačbe:

$$\sigma_{\Theta_c} \propto \frac{1}{\sqrt{N}}.$$

Napaka je obratno sorazmerna s korenom števila izsevanih fotonov. Da bo napaka meritve Čerenkovega kota čim majnša, želimo, da nabiti delec izseva čim več fotonov ob preletu materiala.

7.3.2 Zmajnšanje napake pri meritvi Čerenkovega kota

Ko nabiti delec leti skozi material na različnih mestih, izseva fotone. V primeru tankega materiala je število izsevanih fotonov majhno, a so fotoni izsevani na približno enakem mestu. Čerenkov obroč je tanek (slika 7.5 zgoraj). Če vzamemo debelejši material, bo število izsevanih fotonov večje, vendar bo Čerenkov obroč debelejši (slika 7.5 sredina). Lahko pa vzamemo kombinacijo dveh materialov, kjer je lomni količnik prvega sloja n_1 majnši od lomnega količnika drugega sloja n_2. S

tem povečamo število izsevanih fotonov in ohranimo oster Čerenkov obroč (slika 7.5 spodaj). V primeru Belle II sta v detektorju Čerenkovih obročev za material uporabljena dva sloja aerogela z lomnima količnikoma $n_1 = 1.045$ in $n_2 = 1.055$.

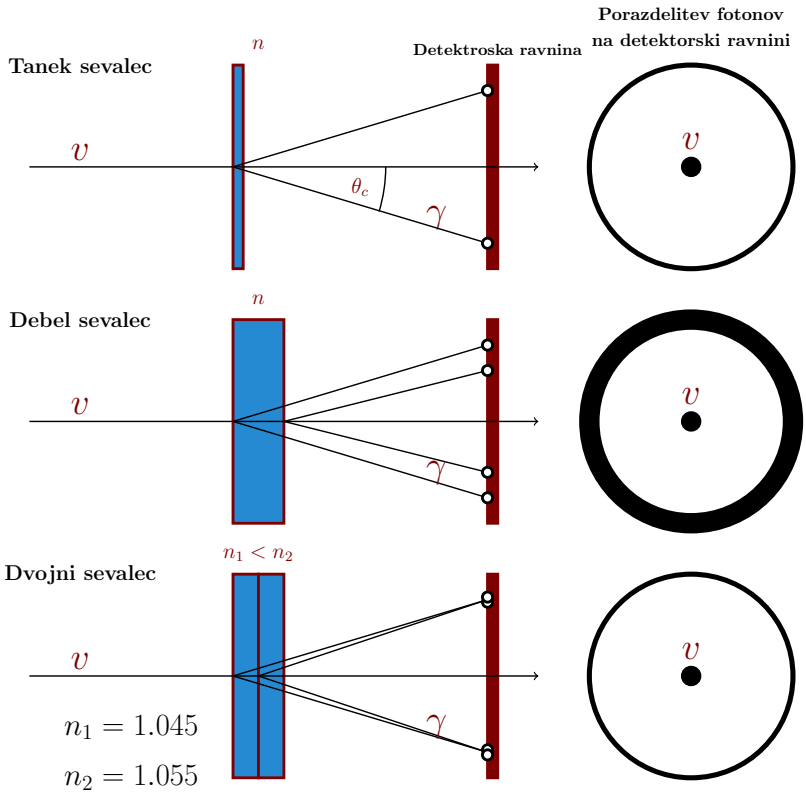

Slika 7.5: Primerjava različnih konfiguracij detektojra za tanek (zgoraj), debel (sredina) in dvojni (spodaj) sevalec. Na sliki (leva stran) so prikazane strukture sevalca in pripadajoči Čerenkovi fotoni, na sliki (desna stran) so prikazani Čerenkovi obroči na detektorski ravnini.

7.3.3 Detektor fotonov

Nastale Čerenkove fotone zaznava pozicijsko občutljiv fotonski detektor. Detektor fotonov mora dobro delovati v magnetnem polju $B = 1.5T$, imeti dobro prostorsko ločljivost za zaznavanje posameznih fotonov in biti odporen na nevtronske poškodbe. Detekor Čerenkovih obročov uporablja module tipa Hybrid Avalanch Photo Diode (HAPD) za zaznavanje posameznih fotonov. HAPD je sestavljen iz štirih APD čipov, ki zaznavajo fotoelektrone. Vsak APD čip ima 36 kanalov. Stranski ris in tloris HAPD sta prikazana na sliki 7.6.

Ko Čerenkov foton zadene kvarčno steklo HAPD, proizvede fotoelektron. Fotoelektron se nato odvrti v močnem električnem in magnetnem polju proti polprevodniškim plazovnim diodam (štiri APD ploščice). Ko fotoelektron zadane plazovno diodo, povzroči v polprevodniku plaz parov in vrzeli. Plaz povzroči električni sunek, preko katerega zaznamo katera dioda je bila zadeta.

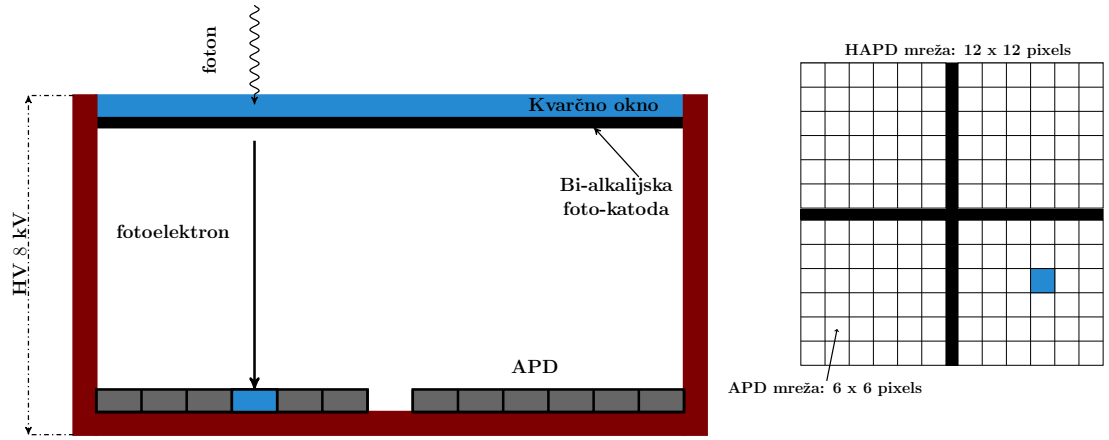

Slika 7.6: Levo: Skica HAPD in konverzija fotona v fotoelektron na kvarčnem steklu. Desno: Mreža HAPD kanalov. Ena četrtina mreže predstavlja APD. Črno območje predstavlja material, ki je neobčutljiv za zaznavanje fotonov. Kanal obarvan z modro predstavlja pozicijo zadetka fotoelektrona.

7.3.4 ARICH

Detektor Čerenkovih obročov ali Aerogel ring Imaging Cherenkov counter (ARICH) je sestavljen iz 420 fotonskih detektorjev HAPD in 124 dvojnih kosov aerogela. Elektronika fotonskih detektorjev poskrbi, da se meritve prenesejo na podatkovne diske. Izgled obeh slojev Čerenkovega detektorja je prikazan na sliki 7.7.

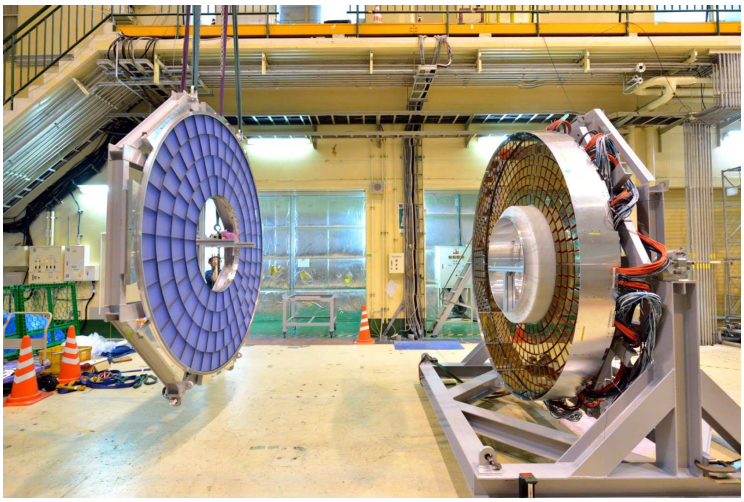

Slika 7.7: Sestava slojev ARICH: ravnine aerogela in ravnine fotonskega detekroja [1].

Poddetektor ARICH je eden izmed dveh sistemov v spektrometru Belle II, ki uporablja Čerenkov efekt za identifikacijo delcev. ARICH s pomočjo Čerenkovega efekta določi identiteto kaonom in pionom z gibalnimi količinami med 0.5 in 4 GeV/c. Za nižje gibalne količine med 0.5 in 1 GeV/c se lahko ARICH poddetektor uporabi tudi za ločevanje med mioni in pioni.

Pri določanju identitete delcev se ARICH opre na uporabo logaritma funkcije maksi-

malnega verjetja L (po angleško Maximum likelihood function). Ob sestavi funkcije $\log(L)$ je zelo pomembno, kako dobro poznamo delovanje poddetektorja ARICH. Da lahko zagotovimo dobro poznavanje delovanja poddetektorja ARICH, je potrebna konstantna kalibracija.

7.3.5 Porazdelitev po Čerenkovem kotu

Kot smo že omenili, vsak nabit delec izseva več fotonov. Za vsakega od izsevanih fotonov lahko izračunamo Čerenkov kot, če poznamo razdaljo med ravnino aerogela in ravnino fotonskega detektorja ter pozicijo fotona na detektorju (glej sliko 7.8).

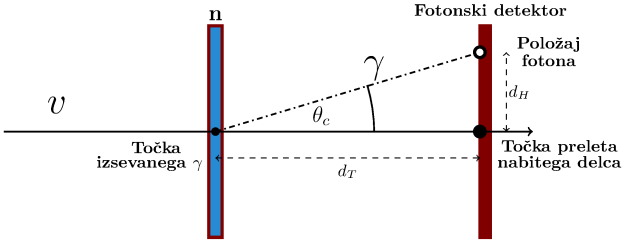

Slika 7.8: Foton zadane fotonski detektor pod določenim kotom θ_c napram točki, iz katere je bil izsevan.

Če za vse zaznane fotone izračunamo Čerenkov kot, lahko izrišemo Čerenkovo porazdelitev (slika 7.9).

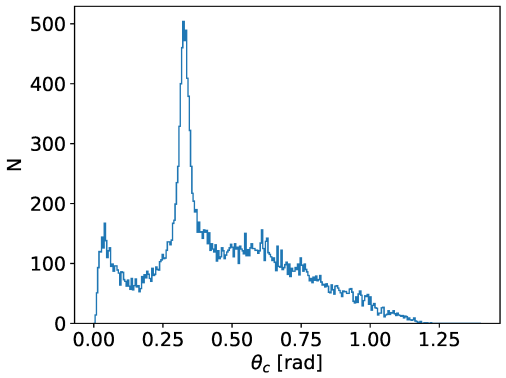

Slika 7.9: Primer Čerenkove porazdelitve za fotone, ki nastanejo ob preletu različnih delcev skozi poddetektor ARICH.

7.3.6 Model Čerenkove porazdelitve

Izmerjena porazdelitev Čerenkovega kota je modelsko najbolj podobna kombinaciji dvojnega Gaussa in linearnega ozadja:

$$g_s(x) = ae^{-\frac{(x-\theta_{c_1})^2}{\sigma_1^2}} + be^{-\frac{(x-\theta_{c_2})^2}{\sigma_2^2}} \qquad g_b(x) = cx + d,$$

kjer parametre $a, b, c, d, \theta_{c_1}, \theta_{c_2}, \sigma_1, \sigma_2$ določimo s prilagoditvijo modela izmerjenim podatkom. Celoten model porazdelitve:

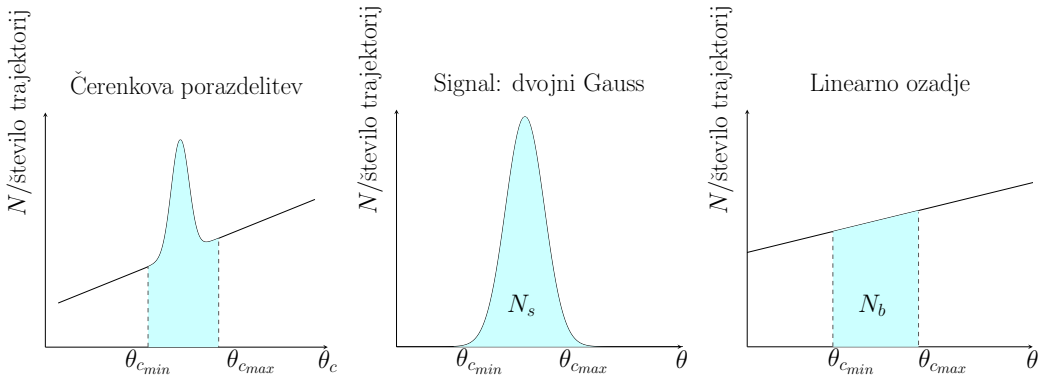

Slika 7.10: Levo: Celotna izmerjena Čerenkova porazdelitev. Sredina: Porazdelitev ozadja. Desno: Porazdelitev signala.

$$g(x) = g_s(x) + g_b(x).$$

Širina porazdelitve nam poda ločljivost Čerenkovega kota, pozicija vrha pa Čerenkov kot. V naših meritvah želimo zagotoviti, da bo ozadje Čerenkove porazdelitve čim majnše. Zmajnšanje ozadja dosežemo s postopkom kalibracije detektorja.

Če sedaj prilagodimo izbrani model izmerjeni Čerenkovi porazdelitvi, lahko s pomočjo dobljenih parametrov modela ocenimo količino signala N_s (slika 7.10 desno):

$$\langle N_s \rangle = \int_{\theta_{c_{min}}}^{\theta_{c_{max}}} g_s(x)dx$$

in količino ozadja N_b (slika 7.10 sredina):

$$\langle N_b \rangle = \int_{\theta_{c_{min}}}^{\theta_{c_{max}}} g_b(x)dx$$

okoli povprečnega Čerenkovega kota. Meje integrala so definirane kot $\theta_{c_{min}} = \theta_{mean} - \sigma_{\theta_c}$ in $\theta_{c_{max}} = \theta_{mean} + \sigma_{\theta_c}$.

7.3.7 Izboljšava razmerja S/B

Vpeljimo še razmerje med signalom in ozadjem:

$$\mathrm{SB} = \frac{N_s}{N_b}$$

in količino, s katero merimo, ali se je razmerje signal/ozadje izboljšalo:

$$\mathrm{SB}_{\text{izboljšava}} = \mathrm{SB}_{\text{ pred rezom}} - \mathrm{SB}_{\text{po rezu}}$$

Rez predstavlja spremembo specifičnega parametra v procesiranju meritev poddetektorja ARICH. Ob spremembi določenega parametra odstranimo določene izmerjene fotone. V postopku kalibracije si ogledamo dva tipa kalibracijskih rezov:

- število, ki določi, kdaj je nek kanal vroč in
- maksimalno število fotonov na APD modulu, ki jih pričakujemo od Čerenkovih obročev.

7.3.8 Model ozadja

S pomočjo rezov odstranimo določeno količino fotonov. Vendar moramo biti zelo pazljivi pri določanju rezov, da ne odstranimo fotonov, ki predstavljajo signal (Čerenkove fotone). Če z našimi rezi odstranimo Čerenkove fotone, ozadje ne bo več linearno (slika 7.11 desno), ampak bo vsebovalo majhen Gausovski vrh. V primeru, da ne odstranimo nič signala, bo ozadje linearno (slika 7.11 levo).

Za potrebe nadaljnje analize želimo razviti program, ki bo omogočal, da določimo, ali je ozadje linearno ali ne. Da lahko ločimo med nelinearnim in linearnim ozadjem, prilagodimo ozadju linearen model med $\theta_c \in [0.1, 0.5]$. Ujemanje med modelom in odstranjenim ozadjem določimo s pomočjo testa χ^2.

Če želimo potrditi ujemanje modela s p parametri in odstranjenega ozadja razdeljenega v N razredov z 99% verjetnostjo, potrebujemo vrednost statistike χ^2 z $N - p - 1$ prostostnimi stopnjami:

$$\chi^2_{correct} = \chi^2_{>99\%}(N - p - 1),$$

kjer vrednost $\chi^2_{correct}$ odčitamo iz tabel poljubnega matematičnega priročnika.

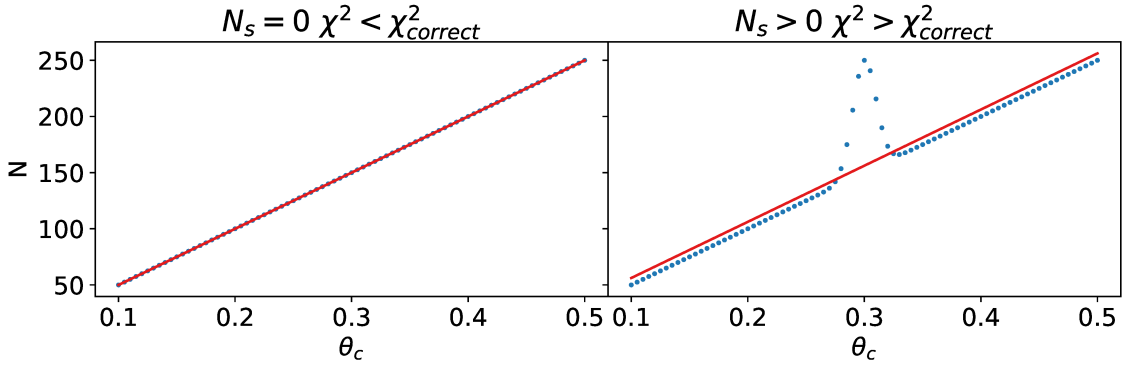

Slika 7.11: Levo: Ozadje, ki ne vsebuje fotonov, ki pripadajo signalu. Desno: Ozadje z Gavsovskim vrhom, ki vsebuje fotone, ki pripadajo signalu.

7.4 Rezultati

Leta 2018 je Belle II pričel s prvimi meritvami. Ob začetku obratovanja ARICH-a je bilo opaženo, da na ločljivost meritev vplivajo naslednji procesi:

1. izmaknjenost detektorja,
2. vroči in mrtvi kanali fotonskega detektorja,
3. fotonski bliski, kjer zasveti celoten modul APD oz. 1/4 HAPD.

Če ugotovimo, kako odstraniti zgornje procese, lahko izboljšamo ločljivost detektorja. Z izboljšanjem ločljivosti se izboljša identifikacija nabitih delcev. V nadaljevanju se osredotočimo na določanja vročih kanalov in fotonskih bliskov.

Za potrebe kalibracije detektorja ARICH je bil razvit set programskih orodji. Analiza je potekala v programskem okolju Belle analysis software framewrok 2 `basf2`, ki je kombinacija programskih jezikov `python` in `C++`. Procesiranje večjih količin podatkov je potekalo na računalniških gručah KEK CC na Japonskem.

Podatki, ki so bili uporabljeni tekom kalibracije, so shranjeni v pozameznih merskih kampanjah (angleško run). Tekom posamezne merske kampanje so bile nastavitve spektrometra Belle II enake. Vse selekcije podatkov, ki jih uporabljamo v nadaljnji analizi, je pripravila delovna skupina Belle II, zadolžena za procesiranje podatkov.

7.4.1 Vroči kanali

Najprej določimo kanale, ki zaznavajo fotone prepogosto (vroči kanali).

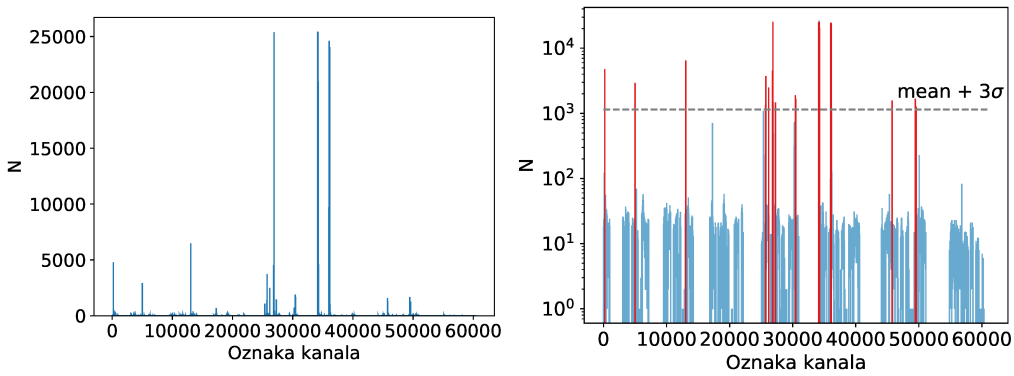

Slika 7.12: Merska kampanja `2018-exp3-01869`. Levo: število fotonov na posamezni kanal. Desno: Kanali, ki presežejo mean $+ 3\sigma$, so označeni z rdečo.

Če preštejemo, koliko zadetkov ima posamezen kanal tekom ene merske kampanje, lahko izračunamo:

- mean: povprečno število zadetkov na posamezni kanal,
- σ: razpršenost števila zadetkov na posamezni kanal,
- vsak kanal, ki ima več zadetkov kot:

$$\text{meja za vroč kanal} = \text{mean} + 3\sigma$$

, proglasimo za vroč kanal.

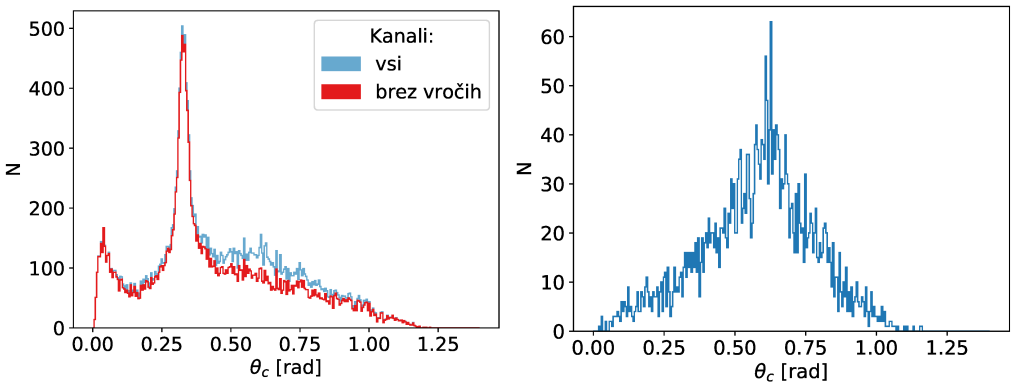

Slika 7.13: Levo: Primerjava Čerenkove porazdelitve za vse fotone in porazdelitve brez fotonov, ki jih zaznajo vroči kanali. Desno: Razlika med Čerenkovima porazdelitvama na levi sliki.

Iz slike 7.12 levo vidimo, da imajo posamezni kanali mnogo več zadetkov kot preostanek kanalov. Če odstranimo Čerenkove fotone, ki jih zaznajo vroči kanali, se Čerenkova porazdelitev spremeni (slika 7.13 levo). Razlika je ozadje, prikazano na sliki 7.13 desno. Izkaže se, da z mejo za vroč kanal = mean + 3σ v nekaterih merskih kampanjah odrežemo tudi fotone, ki pripadajo signalu. Ker tega ne želimo, smo razvili alternativen postopek za določanja vročih kanalov.

Occupancy (pogostost zadetosti)

Za potrebe bolj natančne določitve meje, kdaj je kanal vroč, vpeljemo occupancy oz. pogostost zadetosti. Zanima nas, kako pogosto je posamezni kanal zadet v določeni merski kampanji. Occupancy definiramo kot število zadetkov na kanal v posamezni merski kampanji deljeno s številom vseh dogodkov v merski kampanji:

$$\text{occupancy} = \frac{\text{št. zadetkov na kanal na mersko kampanjo}}{\text{št. dogodkov na mersko kampanjo}}$$

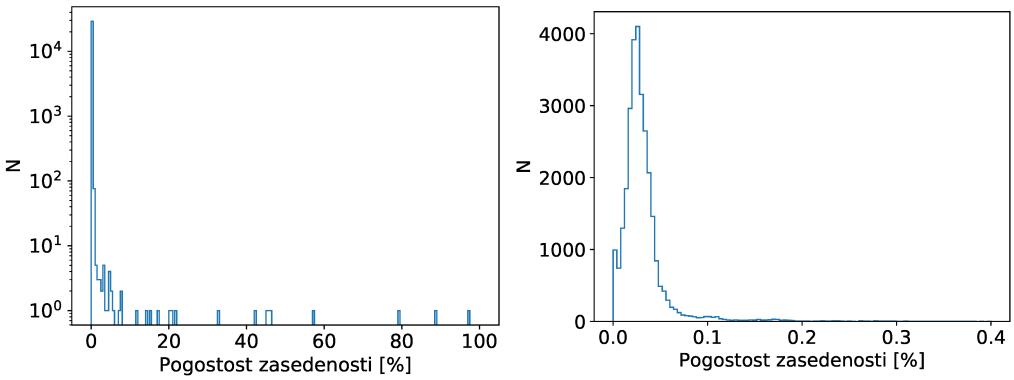

Slika 7.14: Merska kampanja `2018-exp3-02475`. Levo: Celotno območje porazdeliteve zadetosti. Desno: Porazdelitev zadetosti za območje $[0, 0.4]\%$.

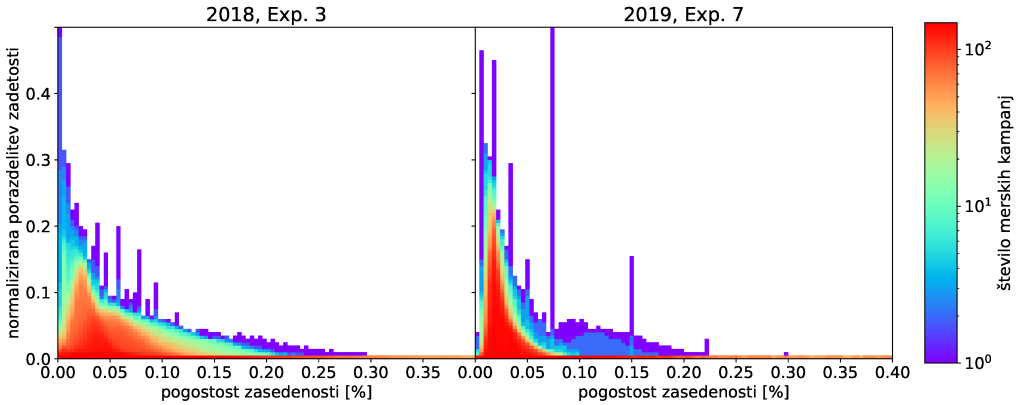

Slika 7.15: Primerjava porazdelitev zadetosti za vse meritve eksperimenta 3 iz leta 2018 (levo) in eksperimenta 7 iz leta 2019 (desno).

Nadalje nas zanima, kolikšna količina kanalov ima velik occupancy in kolikšna količina kanalov ima majhen occupancy. Če occupancy za vse kanale razporedimo v histogram (slika 7.14 levo), dobimo porazdelitev zadetosti. Iz dobljene porazdelitve vidimo, da ima večina kanalov malo zadetkov, nekateri kanali pa veliko zadetkov na mersko kampanjo. Za mersko kampanjo `2018-exp3-02475` so kanali, ki imajo occupancy večji od 1%, najverjetneje vroči.

Poglejmo si še, kakšne porazdelitve zadetosti imajo ostale merske kampanje iz leta 2018 in 2019. Da lahko porazdelitve zadetosti za različne merske kampanje primerjamo med seboj, vsako porazdelitev normiramo s številom aktivnih kanalov posamezne merske kampanje. Če med seboj primerjamo vse porazdelitve zadetosti za merkse kampanje iz leta 2018 in 2019, dobimo sliko 7.15. Barve prikazujejo, kako pogosto se porazdeliteve med sabo prekrivajo. Rdeči del prikazuje del porazdelitve, ki jo ima večina merskih kampanj. Ostale barve nakazujejo, da se porazdelitve zadetosti med seboj nekoliko razlikujejo.

Po primerjavi vseh porazdelitev zadetosti (slika 7.15) predpostavimo, da so vsi kanali, ki imajo occupancy večji kot 0.45%, vroči. Izbrano mejo, ki nam omogoči ločevanje med vročimi kanali in kanali, ki pravilno delujejo, imenujemo največja dovoljena zasedenost (po angleško max. occupancy).

Vsota odstranjenega ozadja

Sedaj želimo preveriti, če z mejo max. occupancy 0.45% odstranimo tudi delež signala. Prva metoda za določanje vsebnosti signala v odstranjenem ozadju je temeljila na uporabi testa χ^2. Izkaže se, da metoda χ^2 ni stabilna in odpove čim se število dogodkov na posamezno mersko kampanjo spremeni za nekaj velikostnih redov. Ker ima test Kolmogorov-Smirnova enak problem kot test χ^2 pri določanju vsebnosti signala v odstranjenem ozadju, smo uporabili nekoliko preprostejšo metodo.

Namesto da preverjamo, ali je signal vseboval ozadje odstranjeno pri posamezni

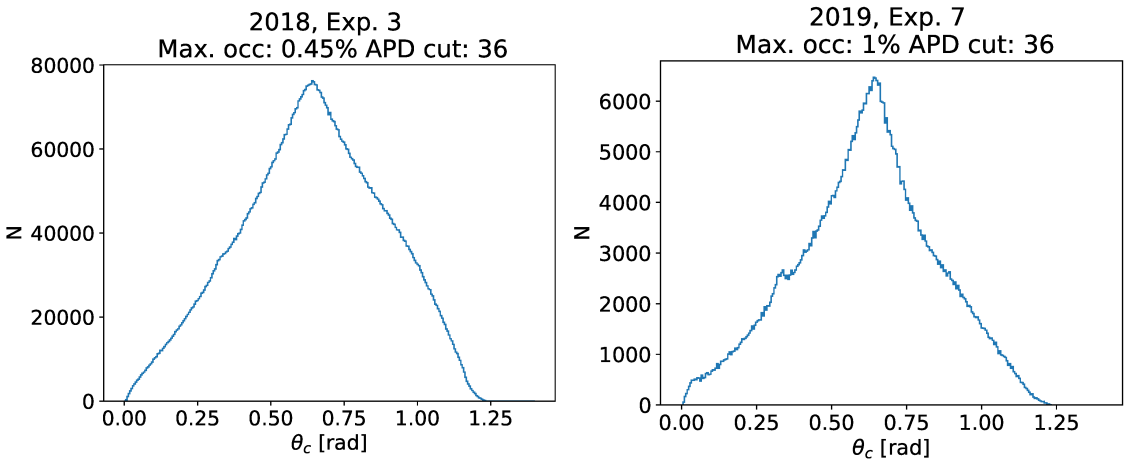

Slika 7.16: Odstranjeno ozadje, h kateremu prispevajo vroči kanali za merske kampanje experimenta 3, 2018 max. occupancy 0.45% (levo) in za merske kampanje experimenta 7, 2019 max. occunapcy 1% (desno).

merski kampanji, enostavno seštejemo vsa odstranjena ozadja za vse merske kampanje posameznega leta. Izkaže se, da je meja max. occupancy 0.45% primerna za odstranitev vročih kanalov za leto 2018. Za leto 2019 pa je bolj primerna meja max. occupancy 1.0%, saj pri meji max. occupancy 0.45% odstranimo nekaj signala.

Porazdelitev ozadja za leto 2018 prikazuje slika 7.16 levo, porazdelitev ozdaja za leto 2019 pa slika 7.16 desno. Porazdelitev ozadja vročih kanalov za leto 2019 sicer še vedno vsebuje nekaj signala. Če postavimo mejo max. occupancy na višjo vrednost, še vedno režemo malo signala. Ker pri vrednosti max. occupancy 1% za leto 2019 odstranimo večino ozadja vročih kanalov, sprejmemo kompromis in se ustalimo na max. occunapncy 1%. Odstranili smo večino ozadja in nekaj malega signala.

Izboljšava S/B razmerja

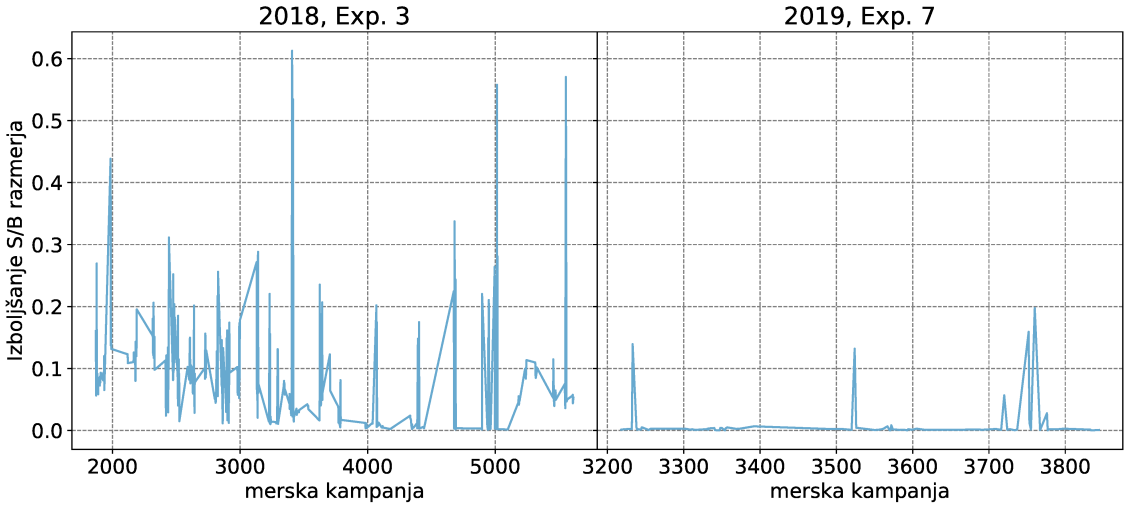

Slika 7.17: Izboljšava razmerja S/B za eksperiment 3 (levo) in eksperiment 7 (desno).

Nadalje nas je zanimalo, če smo z odstranitvijo vročih kanalov izboljšali razmerje med signalom in ozadjem (S/B). Izkaže se, da se v večini primerov S/B razmerje izboljša (slika 7.17). Kadar se S/B razmerje ne izboljša, smo ugotovili, da je bil vzrok:

- merska kampanja z malo odstranjenim ozadjem,
- odstranjeno ozadje ni bilo popolnoma linerano.

Vroči kanali 2018/2019

Preverili smo tudi, koliko vročih kanalov odstranimo iz posamezne merske kampanje z max. occupancy 0.45% za leto 2018 in max. occupancy 1% za leto 2019. Iz slike 7.18 vidimo, da smo v vsaki merski kampanji odstranili kar nekaj vročih kanalov. Opazimo, da je v letu 2019 vročih kanalov manj kot v letu 2018. Omeniti je še potrebno, da je v letu 2018 zaradi težav s hlajenjem delovala le polovica kanalov sistema ARICH. Problem hlajenja je bil konec leta 2018 odpravljen. Od začetka leta 2019 tako deluje celotna ravnina fotonskega detektorja ARICH z vsemi kanali. Znižanje števila vročih kanalov kaže na to, da so operaterji podsistema ARICH izboljšali posamezne detektorske nastavitve, saj je imel celoten ARICH v letu 2019 majn vročih kanalov kot polovica delujočega ARICH-a v 2018.

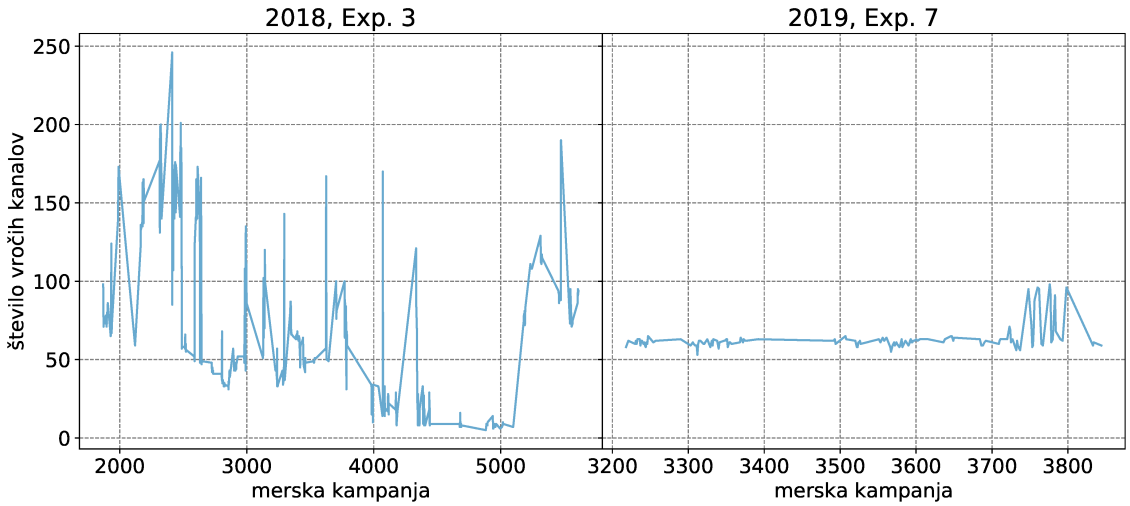

Slika 7.18: Število vročih kanalov pri max. occupancy 0.45% za eksperiment 3 (levo) in max. occupancy 1.0% eksperiment 7 (desno).

7.4.2 APD bliski

Naslednja anomalija, ki smo jo opazili, je, da v določenih trenutkih celoten APD/HAPD modul zasveti (primer bliska slika 7.19). Takega dogodka ne povzroči noben nabit delec, ki bi letel skozi poddetektor ARICH. Nabitih delecv, ki letijo skozi ARICH, je malo in vsak izseva majhno število fotonov.

V nadaljevanju smo želeli ugotoviti, koliko zadetkov na posamezen APD/HAPD modul še predstavlja meritev Čerenkovih obročev in kakšno število zadetkov na

modul predstavlja blisk.

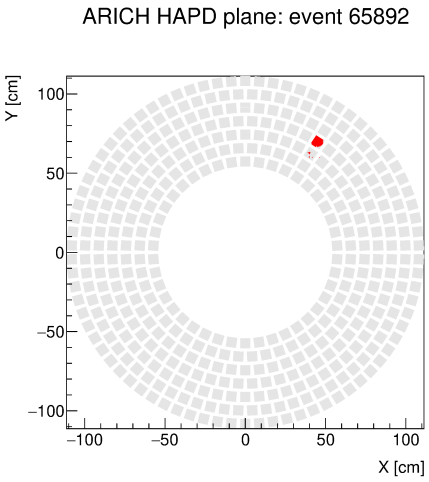

Slika 7.19: Primer bliska, kjer so skoraj vsi kanali na HAPD modulu zaznali foton.

Preverili smo, kako pogosto je zadeto določeno število kanalov na APD/HAPD. Na sliki 7.20 vidimo, da je v kar nekaj primerih zadet celoten HAPD oz. APD. Če si pogledamo, koliko zadetkov ima HAPD pri določenem številu zadetkov na APD, vidimo, da je število zadetkov korelirano. V nadaljevanju gledamo, kako na signal vpliva omejitev števila fotonov na posamezen APD.

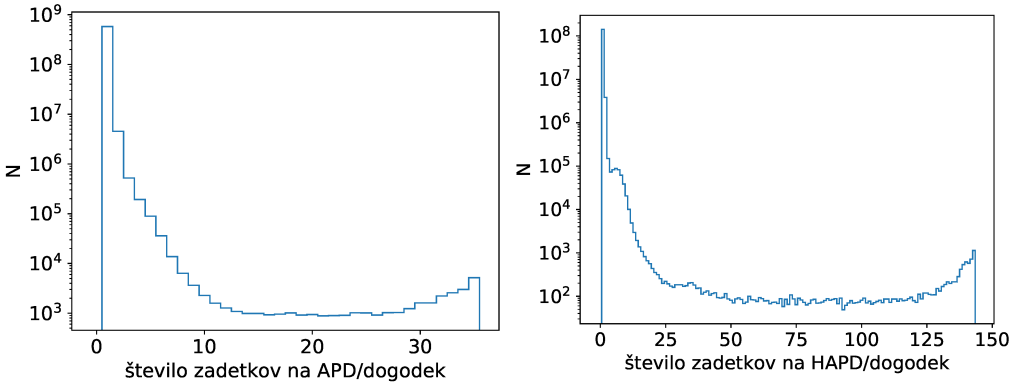

Slika 7.20: Levo: Število zadetkov na APD na dogodek. Desno: Število zadetkov na HAPD na dogodek.

Čerenkova porazdelitev

Za vsako mersko kampanjo nas je zanimalo, kako APD bliski vplivajo na Čerenkovo porazdelitev. Zato smo razklopili odvisnost Čerenkovega kota θ_c od števila zadetkov na APD. Za vsak dogodek smo pogledali, koliko je bilo največje število zadetkov na APD glede na vse APD module na detektorski ravnini. Če je bilo največje število zadetkov na APD v določenem dogodku na primer 26, smo vse fotone dogodka izrisali v 26-ti stolpec histogramain dobili 2D Čerenkovo porazdelitev (slika 7.21).

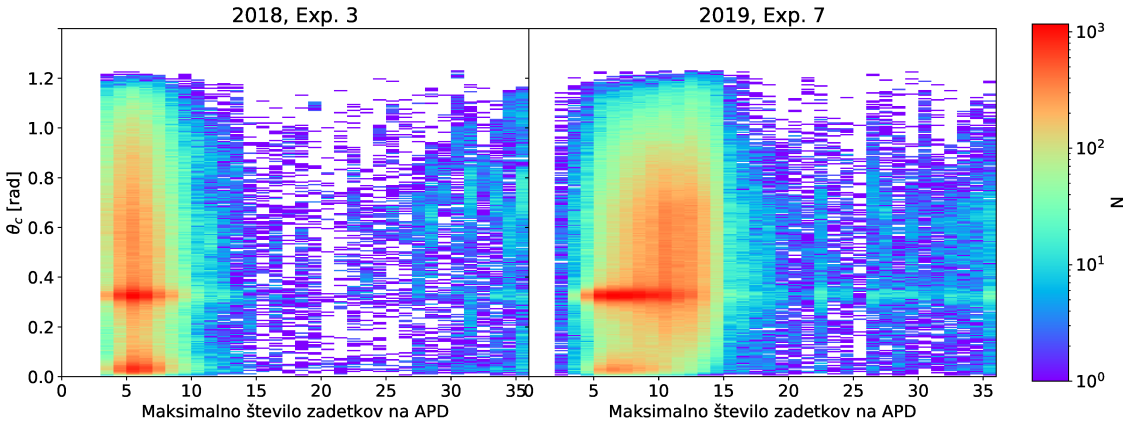

Slika 7.21: Porazdelitev Čerenkovega kota v odvisnosti od maksimalnega števila zadetkov na APD modul (levo) za eksperiment 3 leta 2018 in (desno) za eksperiment 7 leta 2019.

Iz grafa na sliki 7.21 levo vidimo, da se Čerenkova porazdelitev razteza do maksimalno 12 zadetkov na APD za leto 2018 in do maksimalno 16 zadetkov na APD za leto 2019 (slika 7.21 desno). Za odstranitev bliskov izberemo mejo 16 zadetkov na APD modul.

Odstranjeno ozadje

Če sedaj odstranimo fotone, ki jih zaznajo APD moduli s 16 ali več zadetki na APD modul, dobimo porazdelitev ozadja. Iz porazdelitve na sliki 7.22 vidimo, da z odstranitvijo ozadja iz vseh podatkov za eksperiment 3 in 7 nismo odstranili nič signala.

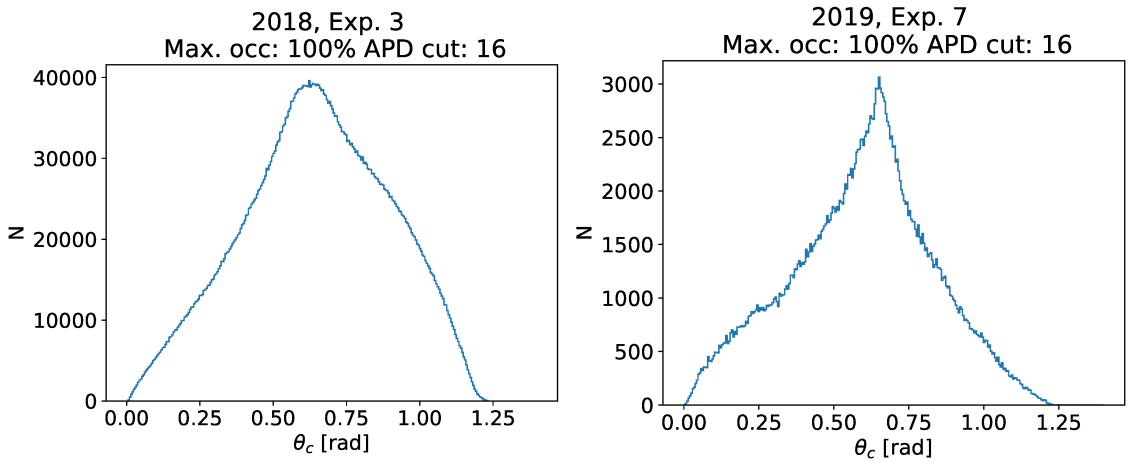

Slika 7.22: Odstranjeno ozadje za APD module, ki so imeli več kot 16 zadetkov na APD za eksperiment 3 (levo) in za eksperiment 7 (desno).

Izboljšava S/B razmerja

Zanima nas še, ali se razmerje S/B kaj izboljša, če odstranimo APD bliske. Ponovno

se izkaže, da za večino merskih kampanj izboljšamo razmerje S/B (slika 7.23). V primerih, kjer se razmerje ne izboljša, gre za merske kampanje, kjer smo odstranili malo ozadja.

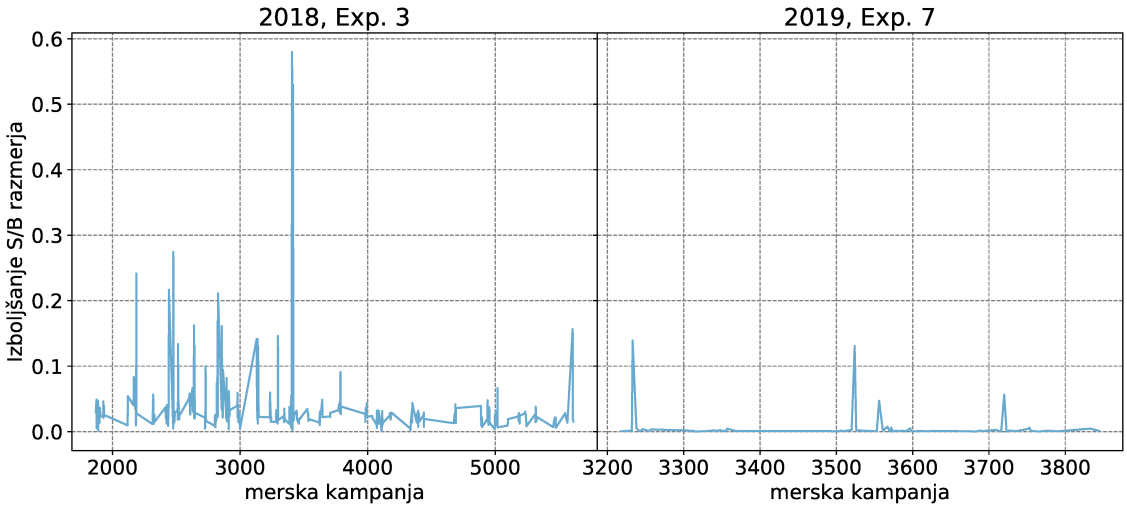

Slika 7.23: Izboljšava razmerja S/B za eksperiment 3 (levo) in eksperiment 7 (desno).

Do sedaj smo si ogledali vpliv vročih kanalov in APD bliskov na vse nabite delce, ki so leteli skozi ARICH. V nadaljevanju si oglejmo še vpliv odstranjenega ozadja na dogodke, kjer ob anihilaciji elektrona in pozitrona nastaneta dva miona ali dva elektrona.

7.4.3 Vpliv na populacijo dogodkov Bhabha $e^+e^- \to e^+e^-$

Ko elektron in pozitron trčita, lahko pride do nastanka novega para elektrona in pozitrona. Tak proces imenujemo sipanje Bhabha.

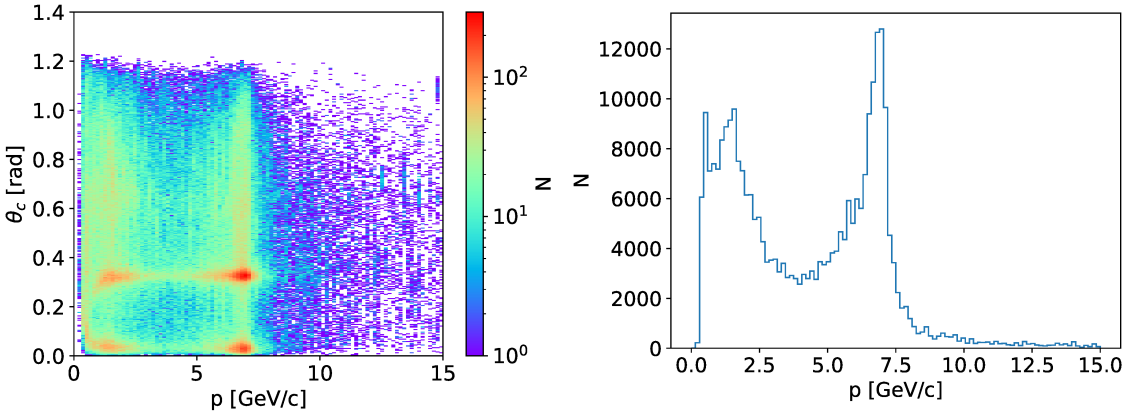

Slika 7.24: Merska kampanja 2018-02475 Levo: Čerenkova porazdelitev v odvisnosti od gibalne količine. Desno: Porazdelitev gibalnih količin za vse nabite delce, ki letijo skozi poddetektor ARICH.

Če izrišemo Čerenkovo porazdelitev v odvisnosti od gibalne količine nabitih delcev, lahko vidimo iz slike 7.24 levo, da je večina Čerenkovih fotonov ali pri gibalni količini

1 GeV/c ali pri gibalni količini 6 GeV/c. Del Čerenkove porazdelitve, kjer je bila gibalna količina večja od 6 GeV/c, so dogodki Bhabha. Da dobimo Čerenkovo porazdelitev za dogodke Bhabha, izrišemo le Čerenkove kote fotonov, ki so jih proizvedli nabiti delci z gibalno količino večjo od 6 GeV/c.

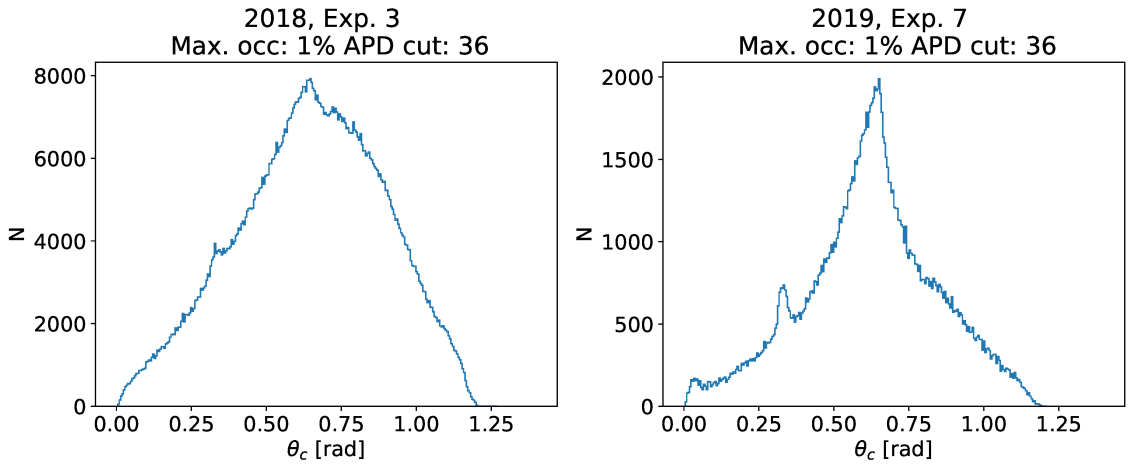

Slika 7.25: Odstranjeno ozadje za eksperiement 3 (levo) in ozadje za eksperiment 7 (desno), ki ga h Čerenkovi porazdelitvi za Bhabha dogodke prispevajo vroči kanali.

Na sliki 7.25 je prikazano ozadje, ki ga odstranimo iz Čerenkove porazdelitve za Bhabha dogodke. V primeru eksperimenta 7 odstranimo nekaj malega signala, a to ni presenetljivo, saj smo podoben efekt opazili že pri Čerenkovi porazdelitvi za vse nabite delce.

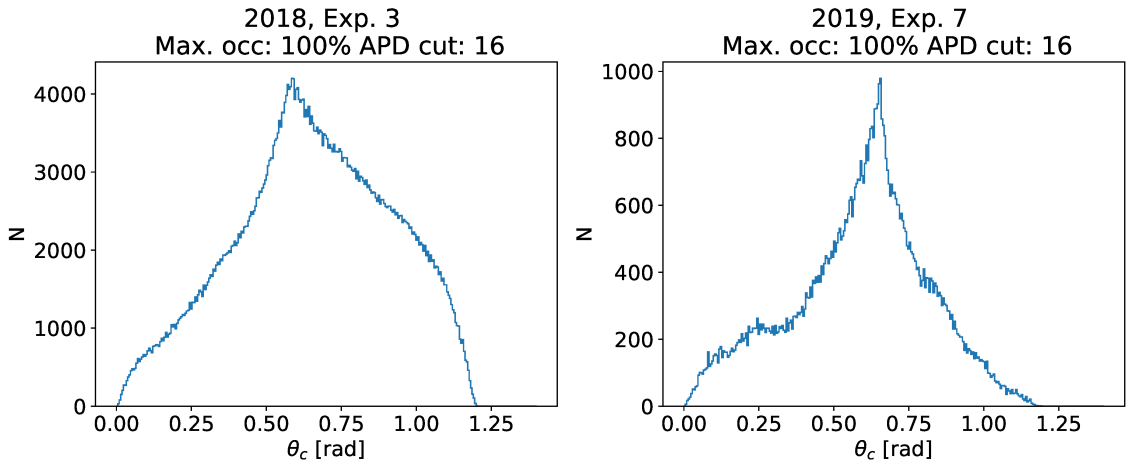

Slika 7.26: Odstranjeno ozadje za eksperiement 3 (levo) in ozadje za eksperiment 7 (desno), ki ga h Čerenkovi porazdelitvi za Bhabha dogodke prispevajo APD bliski.

Na sliki 7.26 vidimo ozadje APD bliskov, ki ga odstranimo iz Čerenkove porazdelitve za Bhabha dogodke. Odstranimo kar nekaj ozadja, a ne odstranimo nobenega signala.

7.4.4 Vpliv na populacijo dogodkov Di-muon $e^+e^- \to \mu^+\mu^-$

Vzorec dogodkov, kjer je ob trku elektrona in pozitrona nastal par mionov $e^+e^- \to \mu^+\mu^-$, je pripravljen s strani delovne skupine Belle II, zadolžene za procesiranje podatkov. Selekcija dogodkov $e^+e^- \to \mu^+\mu^-$ je namreč nekoliko bolj zapletena od selekcije Bhabha dogodkov.

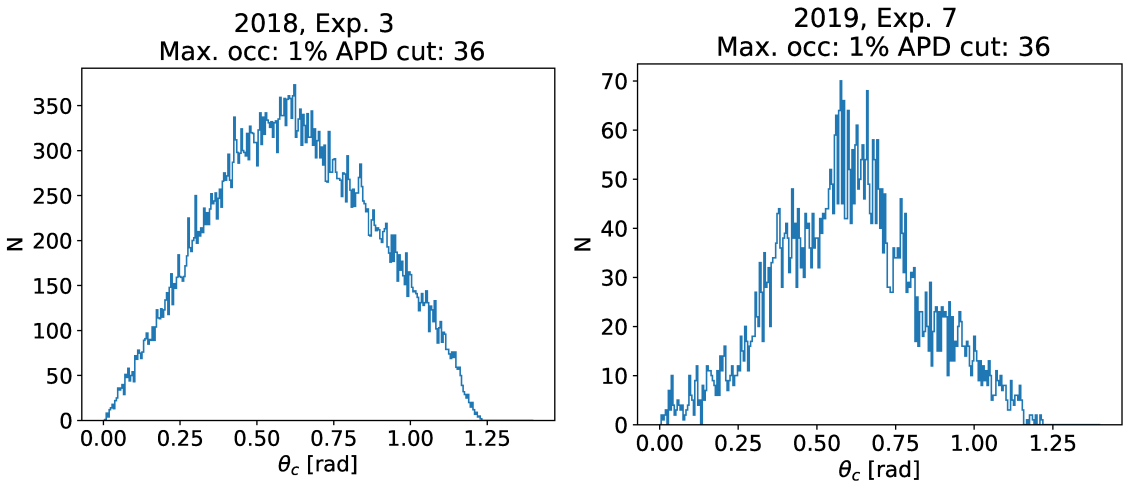

Slika 7.27: Odstranjeno ozadje za eksperiement 3 (levo) in ozadje za eksperiment 7 (desno), ki ga k Čerenkovi porazdelitvi za Di-muon dogodke prispevajo vroči kanali.

Iz slike 7.27 vidimo, da ozadje, ki ga povzročijo vroči kanali, ne vsebuje nobenega signala. Ozadje, h kateremu prispevajo APD bliski (slika 7.28), ni linearno. Dogodkov tipa $e^+e^- \to \mu^+\mu^-$ je mnogo premalo, da bi lahko postavili kakršne koli globlje zaključke, zakaj je ozadje za APD bliske pri di-muon dogodkih takšne oblike.

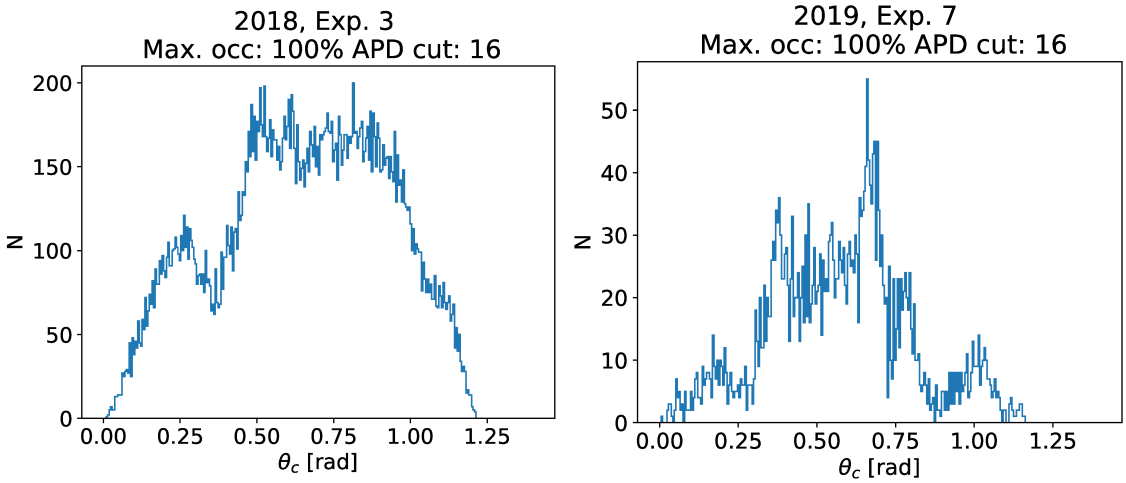

Slika 7.28: Odstranjeno ozadje za eksperiement 3 (levo) in ozadje za eksperiment 7 (desno), ki ga k Čerenkovi porazdelitvi za Di-muon dogodke prispevajo APD bliski.

7.5 Zaključek

V okviru dela smo prišli do naslednjih rezultatov, ki so uporabni za potrebe kalibracijskega procesa poddetektorja ARICH:

- Najbolj primeren model za opis Čerenkove porazdelitve je kombinacija dveh Gaussovih funkcij in linearne funkcije.
- Za odstranitev vročih kanalov moramo iz naših podatkov odstranit fotone, ki pripadajo kanalom, katerih zasedenost je bila večja od:
  - 0.45% za leto 2018,
  - 1.0% za leto 2019.
- Za odstranitev APD bliskov moramo odstraniti vse primere, kjer je število zaznanih fotonov na APD čip preseglo 16 fotonov za leto 2019.
- Vsota odstranjenih ozadji za vse merske kampanje iz posameznega leta je najboljša metoda, s katero lahko preverimo, ali so rezi vročih kanalov in APD bliskov odstranili kaj singala.
- Potrdili smo, da s predlaganimi rezi res izboljšamo razmerje S/B med signalom in ozadjem v izmerjeni Čerenkovi porazdelitvi.

S pomočjo ugovotitev te naloge bo lahko raziskovalna skupina, zadolžena za obratovanje poddetektorja ARICH, izboljšala obratovanje detektorja v prihodnosti.

Bibliography

[1] Belle II collaboration internal data, `https://confluence.desy.de`, [view 5. 12. 2018].

[2] I. Kaminer, *Photonic crystals, graphene, and new effects in Cherenkov radiation*, 9th International Workshop on Ring Imaging Cherenkov Counters, (2016).

[3] C. Grupen, *Particle detectors*, Cambridge University Press, (2008).

[4] P. Cherenkov, *Visible Radiation Produced by Electrons Moving in a Medium with Velocities Exceeding that of Light*, Phys. Review, **52**, 378 (1934).

[5] I. Frank, I. Tamm, *The coherent radiation of a fast electron in a medium*, Doklady AN SSSR, **14**, 107-112, (1937).

[6] J. V. Jelly, *Cherenkov radiation and its applications*, Pergamon press, (1958).

[7] R. Pestotnik et all, *Calibration of the Belle II Aerogel Ring Imaging Detector*, NIMA, **0168-9002**, 161800, (2019).

[8] Kuhr, T., Pulvermacher, C., Ritter, M. et al. *The Belle II Core Software*. Comput Softw Big Sci 3, 1 (2019) `doi:10.1007/s41781-018-0017-9`.

[9] R. Brun, F. Rademakers, *ROOT - An Object Oriented Data Analysis Framework*, Proceedings AIHENP'96 Workshop, (1996).